

The 2023 Australian Total Solar Eclipse: Line Emission of Fe XIV, Fe X and Fe XI out to 6 solar radii

BENJAMIN BOE,¹ SHADIA HABBAL,² MILOSLAV DRUCKMÜLLER,³ PAVEL ŠTARHA,³ MATĚJ ŠTARHA,³ JANA HODEROVÁ,³
SAGE CONSTANTINOU,² ERIC AYARS,⁴ AND DANIELL CASILLAS⁴

¹*Wentworth Institute of Technology, Boston, MA 02115, USA*

²*Institute for Astronomy, University of Hawaii, Honolulu, HI 96822, USA*

³*Faculty of Mechanical Engineering, Brno University of Technology, Technická 2, 616 69 Brno, Czech Republic*

⁴*Department of Physics, California State University, Chico, CA 95929, USA*

ABSTRACT

We present narrowband observations of the Fe XIV (530.3 nm), Fe X (637.4 nm), and Fe XI (789.2 nm) coronal emission lines from the 2023 April 20 Total Solar Eclipse in Australia. We deployed pairs of telescopes for each emission line that were equipped with narrowband filters centered on, and several nanometers away from, the center wavelengths of the lines. The secondary continuum telescopes were used to measure and remove the combined continuum K- (electron) and F- (dust) corona, which dominate coronal emission at optical and infrared wavelengths. Significant emission was detected from all three lines from 1.03 solar radii (R_{\odot}) continuously outward to at least 6 R_{\odot} . The brightness of the lines and continuum are absolutely calibrated to the solar disk, and are validated by a comparison with LASCO-C2 observations made at the same time. Using these observations, we inferred the line emission ratios resolved throughout the middle-corona (defined as 1.5 to 6 R_{\odot}) for the first time. These line ratios are a probe of the electron temperature, which have important implications for constraining models of coronal heating and the characterization of solar wind formation, yet these emission lines have scarcely been quantified beyond 3 R_{\odot} in the corona. This study demonstrates the enduring potential of eclipse observations for coronal physics and suggests that future spacecraft missions could observe these lines farther out than has been attempted previously.

Keywords: Solar physics (1476), Solar corona (1483), Solar eclipses (1489), Solar optical telescopes (1514), Solar coronal streamers (1486), Solar cycle (1487)

1. INTRODUCTION

Observations of ionic emission lines have long been used to characterize the physical properties of the solar corona. Ionic line emission was first observed in the corona during the 1869 Total Solar Eclipse (TSE) by C. A. Young (1872), using a slit-less spectrum (similar to the modern reproduction shown in the bottom right panel of Figure 1). Originally thought to be a new element named “Coronium”, this “Green” line at 530.3 nm, as well as the “Red” coronal line at 637.4 nm, were subsequently identified as Fe XIV and Fe X respectively by W. Grotrian (1939) and B. Edlén (1943).

For several decades, coronal line emission could only be seen during TSEs until the invention of the coronagraph by Lyot, who then identified several coronal lines (B. Lyot 1939), including a near-infrared line at

789.2 nm of Fe XI. Surveys of Fe XIV (and often Fe X) continued for decades throughout the 20th-century at Lomnický štít, Sacramento Peak, and others (e.g., M. Rybansky et al. 1994; R. C. Altrock 2011; J. Oloketuyi et al. 2024), albeit at a low coronal height of 1.15 solar radii (R_{\odot}). Eclipse-based observations continued as well during this time, though the emission detected was typically below 1.3 R_{\odot} (M. Guhathakurta et al. 1992), with occasional detections out to 1.7 R_{\odot} (J. Singh et al. 1982).

Based on these foundational findings, the Large-Angle Spectrometric CORonagraph (LASCO) C1 coronagraph (LASCO-C1; G. E. Brueckner et al. 1995) onboard the Solar and Heliospheric Observatory (SOHO), included a Fabry-Pérot interferometer to observe these visible-wavelength lines, which produced measurements of the line brightness (Y. M. Wang et al. 1997; N. Srivastava et al. 2000) and line-widths (M. Mierla et al. 2008) of both Fe XIV and Fe X until its premature failure in 1998.

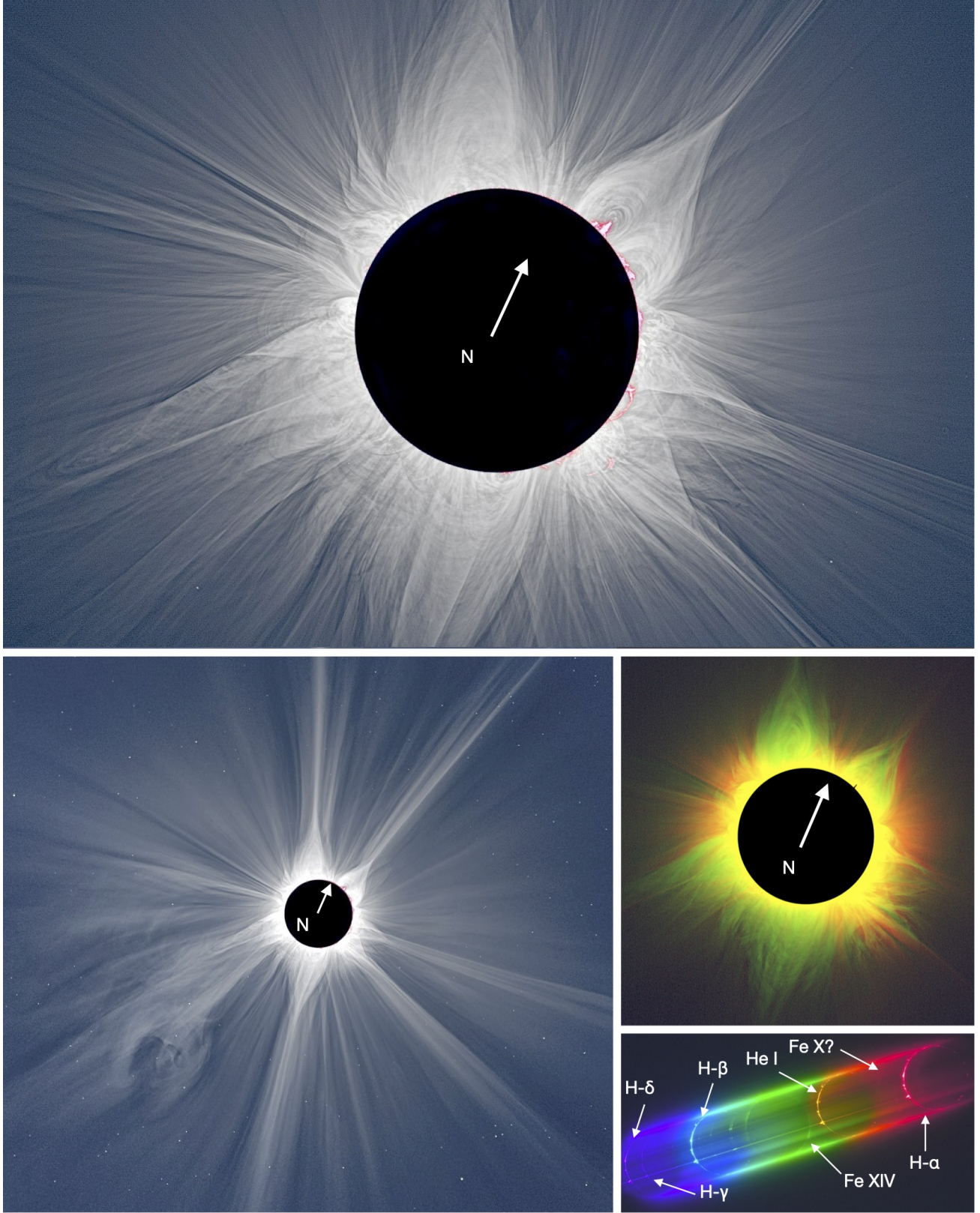


Figure 1. White-light and narrowband images of the corona during the TSE from Exmouth, Australia, on 2023 April 20. The top image was taken with a 1000mm lens, while the bottom-left image shows a wider field-of-view from a 200mm lens (composited with the 1000mm image for the low corona). The middle-right panel shows a composite of Fe XIV (green) and Fe X (red) emission (see Section 2.2). The arrows in each image indicate the direction of solar North. The bottom right panel shows a slit-less flash spectrum of the corona with the strong Hydrogen, Helium, and Iron lines labeled.

These data were still limited in helioprojective height to less than about $2 R_{\odot}$, but demonstrated the strong potential of observing these lines from space.

Much of the focus on these visible wavelength lines diminished in the early 21st century, largely due to the introduction of observations from a wider spectrum of wavelengths. At somewhat shorter wavelengths in the ultraviolet (ranging from ≈ 47 to 135 nm), several coronal ionic lines as well as Lyman Alpha (Ly- α , 121.6 nm) were spectroscopically observed by SOHO's Ultraviolet Coronagraph Spectrometer (UVCS; J. L. Kohl et al. 1995) consistently out to 3.5 - $5 R_{\odot}$ (J. C. Raymond et al. 1997; Y.-K. Ko et al. 1997; R. M. Suleiman et al. 1999; A. Akmal et al. 2001; A. Nakagawa 2008), with some detections in the tips of streamers out to as far as $8 R_{\odot}$ (J. L. Kohl et al. 1997).

The new coronagraph Metis (E. Antonucci et al. 2020) on Solar Orbiter has expanded these observations, imaging Ly- α emission out to $7 R_{\odot}$ in streamer tips near solar-minimum (M. Romoli et al. 2021), and from CME material out to heights as much as $9 R_{\odot}$ (which is claimed to translate to $23 R_{\odot}$ after accounting for projection effects; G. Russano et al. 2024).

While Ly- α is the strongest resonantly excited line in the corona, and provides a useful method for probing the solar wind speed due to the ‘‘Doppler-dimming’’ effect (e.g., C. L. Hyder & B. W. Lites 1970; G. L. Withbroe et al. 1982; J. L. Kohl et al. 1998; S. Giordano et al. 2025), it cannot directly probe the electron temperature, unlike what is achievable with ionic line emission from heavier elements. Still, it may be possible to use polarized observations of Ly- α to measure the magnetic field strength via the Hanle effect, though likely only near active regions (N. E. Raouafi et al. 2016; H. D. Supriya et al. 2021).

Now equipped with space-based telescopes, observations at Extreme Ultraviolet (EUV) and X-ray wavelengths have ushered in a new era of coronal astronomy. The abundant quantities of these data in the lower regions of the corona (often below $1.5 R_{\odot}$) have proven exceptionally useful for a wide range of applications (see G. Del Zanna & H. E. Mason 2018 and ref. therein). In particular, these observations have helped inform coronal heating and solar wind acceleration models by constraining the electron temperature distributions in various structures (see N. M. Viall et al. 2021), and to investigate the initiation of coronal mass ejections (CMEs; see B. J. Thompson et al. 2021) and other complex dynamics near the Sun.

One drawback of emission at EUV and X-ray wavelengths in particular is that they fade much more rapidly with heliocentric distance than do lines at near-UV, visi-

ble, and infrared wavelengths. Low down in the corona, collisions between electrons and ions cause lines to be excited regardless of incoming radiation. Farther out in the corona (typically at about 1.5 to $2.5 R_{\odot}$; e.g., S. R. Habbal et al. 2007; D. B. Seaton et al. 2021; B. Boe et al. 2022), the rate of collisions drops dramatically due to the steep drop off in density with heliocentric distance, and so the emission generated by collisions reduces dramatically. While the brightness from collisional excitation depends on the density squared ($\propto n_e^2$; requires two particle interaction), the brightness due to radiative excitation depends linearly on density ($\propto n_e$). So, for wavelengths in the near-UV, visible, and infrared, the solar photosphere offers an abundant source of incident radiation to excite the lines, enabling them to be observed out to high helioprojective distances (e.g., S. R. Habbal et al. 2010c, 2011).

There is some radiative excitation of the EUV lines due to radiation generated lower down in the corona by collisions, which does enable some EUV detection out to as much as $6 R_{\odot}$ (D. B. Seaton et al. 2021; F. Auchère et al. 2023; G. Del Zanna 2025). Still, the EUV emission at heights above $2 R_{\odot}$ is exceptionally weak (requiring longer exposure times to observe) and is confined mostly to streamer tips. Further, the incoming radiation from lower down in the corona is highly angle-dependent and temporally variable (D. B. Seaton et al. 2025), making the emission difficult to use as a robust physical diagnostic. Thus, the strongly radiatively excited lines at longer wavelengths still offer an important contribution to the study of the solar corona, filling in parts of the corona beyond 1.5 - $2 R_{\odot}$ that are difficult to probe with EUV alone.

Furthermore, a large variety of powerful diagnostics have been demonstrated in recent years to utilize these radiatively excited lines. Comparing the relative emission of these lines provides information on the electron temperature (T_e) distribution along the line-of-sight (LOS; e.g., S. R. Habbal et al. 2010a, 2021; B. Boe et al. 2023a), via the ionization equilibrium abundances of the different ions (as plotted in Figure 2 for Fe X, Fe XI, and Fe XIV). The widths of the lines can reveal non-thermal motions (e.g., M. Mierla et al. 2008; S. Koutchmy et al. 2019; G. D. Muro et al. 2023; Y. Zhu et al. 2024) as well as the ion temperatures (R. Esser et al. 1999). The Doppler shift of the line center makes it possible to infer the bulk motions along the LOS (e.g., M. Mierla et al. 2008; Y. Zhu et al. 2024), while the time variability in the Doppler shift and intensities can be used to infer the properties of coronal waves (S. Tomczyk et al. 2007; R. J. Morton et al. 2025; M. Hahn et al. 2025). Changes in the emission and

Doppler signature of the lines also enable studies of the dynamics and propagation of Coronal Mass Ejections (CMEs; e.g., N. Srivastava et al. 2000; A. Akmal et al. 2001; A. Ding & S. R. Habbal 2017; B. Boe et al. 2020), which is now being explored from space with the Visible Emission Line Coronagraph (VELC) on Aditya-L1 (R. Ramesh et al. 2024; V. Muthu Priyal et al. 2025). The polarization of the line profile can even provide constraints on the coronal magnetic field direction (S. Tomczyk et al. 2008; S. E. Gibson et al. 2017) and strength (for lines in the infrared; H. Lin et al. 2004; T. A. Schad et al. 2024a).

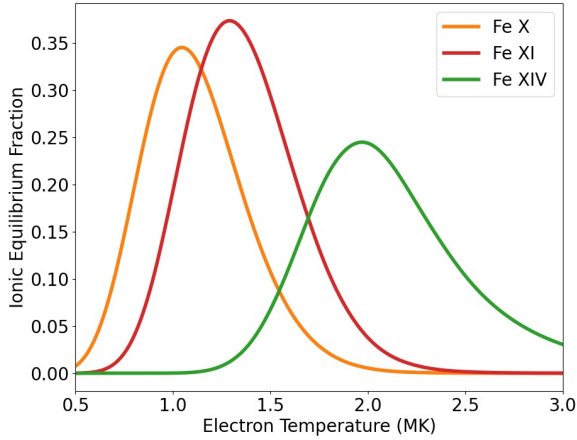


Figure 2. The ionization equilibrium abundances of Fe X, Fe XI, and Fe XIV as a function of T_e . Data are shown as spline interpolated values from the CHIANTI database (K. P. Dere et al. 1997; R. P. Dufresne et al. 2024).

Nonetheless, observing line emission at visible and infrared wavelengths also has its drawbacks (which are different than those for EUV lines), namely that coronal emission at those wavelengths is dominated by continuum scattering of the K-corona (Thompson scattering by electrons) and F-corona (interplanetary dust scattering, becomes the Zodiacal light at large elongation angles; see I. Mann 1998). The K-corona itself is useful for measuring the coronal density, after the F-corona emission is removed. The K- and F-corona are typically separated from each other by a polarization method of white-light emission (H. C. van de Hulst 1950), but recent work demonstrated that they can also be separated using a color-based method (since the F-corona is red in color; B. Boe et al. 2021).

Comparing the line emission profiles as a function of helioprojective distance along structures to the corresponding continuum emission from the K-corona additionally facilitates a method for inferring the distance at which the ions freeze-in to a fixed ionization state as they flow outward into the solar wind (S. R. Habbal

et al. 2007, 2011; B. Boe et al. 2018). So even though the K- and F-corona brightness requires instrumental considerations to remove from the line emission, it does enable additional physical inferences which expand the potential of such data.

Despite the unique advantages of emission lines at visible and near-infrared wavelengths, a majority of the observations at those wavelengths in recent years have focused on the continuum emission for the sake of inferring the structure and changes in the coronal density (e.g., the Wide-field Imager for Solar Probe, WISPR A. Vourlidas et al. 2016, and the Polarimeter to UNify the Corona and Heliosphere, PUNCH, C. Deforest et al. 2022). While that information is incredibly useful, particularly when there is time variability to study CMEs and other transient features, it does not provide information on the T_e or elemental abundances, which are essential for answering questions about the heating of the corona and the exact formation processes of the solar wind. Even so, some information on T_e can be extracted by narrowband polarized brightness observations of the K-corona around 400 nm (with the CORonal Diagnostic EXperiment, CODEX, N. Reginald et al. 2023). Observations of the ionic emission over the same coronal region could, in combination with this method, be used to validate the calibration of such observations and could be used to distinguish any differences between the thermal and ionization temperature, which could be valuable for constraining non-equilibrium processes in the corona.

Recent observations have also been pushing the capabilities of detecting visible and near-infrared emission out to larger heights in the corona. B. Boe et al. (2022) demonstrated emission from the visible and near-infrared lines of Fe XIV, Fe X, and Fe XI out to as much as $3.4 R_\odot$ during solar-minimum (at the end of Solar Cycle 24), making the extent comparable to the UVCS measurements of ionic line emission. In this work, we present these same three lines observed during the 2023 April 20 TSE, close to the maximum of Solar Cycle 25, continuously outward from just above the solar disk out to $6 R_\odot$ – probing ionic line emission throughout the entire middle-corona (from 1.5 to $6 R_\odot$, M. J. West et al. 2023) for the first time.

In Section 2, we discuss the eclipse expedition and describe the instrumentation deployed in Australia, while detailed descriptions of the data reduction, processing, and calibration are included in Appendix A. In Section 3, we review the observations and initial findings of the line emission (Section 3.1 and 3.2), the corresponding continuum emission near each line (Section 3.3). A discussion of the key findings can be found in Section 4.

2. THE 2023 TOTAL SOLAR ECLIPSE EXPEDITION

The 2023 April 20 TSE occurred during the rising phase of Solar Cycle 25 near the peak of solar activity. The eclipse was hybrid, with totality occurring in parts of Western Australia, East Timor, and parts of Indonesia. Our primary observing site was located in Exmouth, Australia, on the North West Cape (also referred to as the Ningaloo Peninsula), which had our entire complement of white-light and narrowband imaging systems. In Exmouth, totality lasted 53.8 seconds at 03:30 UT (11:30 local time). We had a secondary observing site, with more limited instrumentation comprised of only Fe XIV and Fe XI imaging systems, on a small island in the cluster of Lowendal Islands, approximately 208 km northeast of Exmouth. Totality on the island lasted for 61.9 seconds and occurred at 3:34 UTC (11:34 local time). The secondary site served as a safeguard against possible weather issues at Exmouth, but both sites had excellent observing conditions during totality (zero cloud cover), and so the data from both sites could be combined to increase the coronal signal-to-noise ratio (SNR). At the Exmouth (Island) site, the Sun was at a high altitude of 54.3 (56.3) degrees, creating ideal observing conditions despite the short duration of totality. In fact, the short totality meant that the Moon was nearly the exact same angular size as the Sun in the sky (eclipse magnitude of 1.00443), so almost all of the corona down to the chromosphere could be seen during the entire eclipse.

Indeed, the upper-chromosphere (and prominences) can be seen well in the simple slit-less flash spectrum of the corona taken with a 4K (3840x2160) color video camera (Panasonic HC-X1500, 600mm lens) through a transmission diffraction grating shown in the bottom right panel of Figure 1. The slit-less spectrum shows the Balmer series of Hydrogen lines, the strong Helium line (the yellow 587.6 nm He I line), as well as the green Fe XIV line, representing a modern recreation of the original “Coronium” detection by C. A. Young (1872). There is even some faint emission from what is likely the red Fe X line (just to the left of the bright red H- α line).

We discuss the eclipse instruments used to record the high spatial resolution white-light images in Section 2.1 and the narrowband line emission in Section 2.2. For all observations, we performed standard dark frame subtraction and flat fielding. Dark frames were taken immediately after totality by completely covering the telescopes with both lens caps and towels before running the same exposure sequences used during totality. Flat fields were taken by looking at clear blue sky near zenith

(but away from the Sun to avoid direct illumination) with white translucent plastic coverings on top of the lens (i.e., the cover was out of focus and so recorded the relative optical efficiency throughout the system). The plastic coverings were then rotated in increments of 60 degrees and repeated six times (so every possible angle for the holders) in order to reduce any possible systematics introduced by the flat-fielding procedure.

2.1. White-light Imagers

High-resolution white-light imaging is useful for characterizing the fine-scale structures of the corona. For our observing site in Exmouth, we used a 1000mm lens with a Nikon Z6 II camera to observe the lower portion of the corona, out to about $3 R_{\odot}$. A composite image is shown in the top panel of Figure 1, which is comprised of 77 unique exposures taken during totality. To probe the corona to larger helioprojective distances, we used two identical wide-field telescope systems composed of 200mm lenses with Nikon D810 cameras. For all the white-light telescopes, the exposure times spanned 1/125s up to 1s. A composite of these wider-field observations out to about $10 R_{\odot}$ is shown in the lower left panel of Figure 1, which is made from 199 images from the 200mm cameras as well as the 1000mm observations. The white-light data were aligned using a phase-correlation method as described in M. Druckmüller (2009), and processed to enhance fine-scale features by removing much of the low spatial-frequency signal in the overall drop of coronal brightness with distance from the Sun, as introduced by M. Druckmüller et al. (2006).

These white-light observations display the classic solar maximum shape of the corona (see E. W. Maunder 1899), with coronal streamers occurring at almost all latitudes, intermixed with small open-field corridors (as opposed to a solar minimum corona with large equatorial streamers and polar coronal holes). A small CME was also present in the southwest region of the corona, seen in the wide field image at about 6-8 R_{\odot} .

2.2. Narrowband Imagers

To record the ionic emission lines, we performed observations with a suite of telescopes that were custom-made for this eclipse with modern high-resolution detectors and new narrowband filters. The observations of the line emission for Fe XIV are shown in Figure 3, Fe X in Figure 4, and Fe XI in Figure 5. A qualitative composite of the Fe XIV and Fe X emission is shown in Figure 1.

The narrowband filters were manufactured by the Aluxa corporation with bandpasses with a full width at

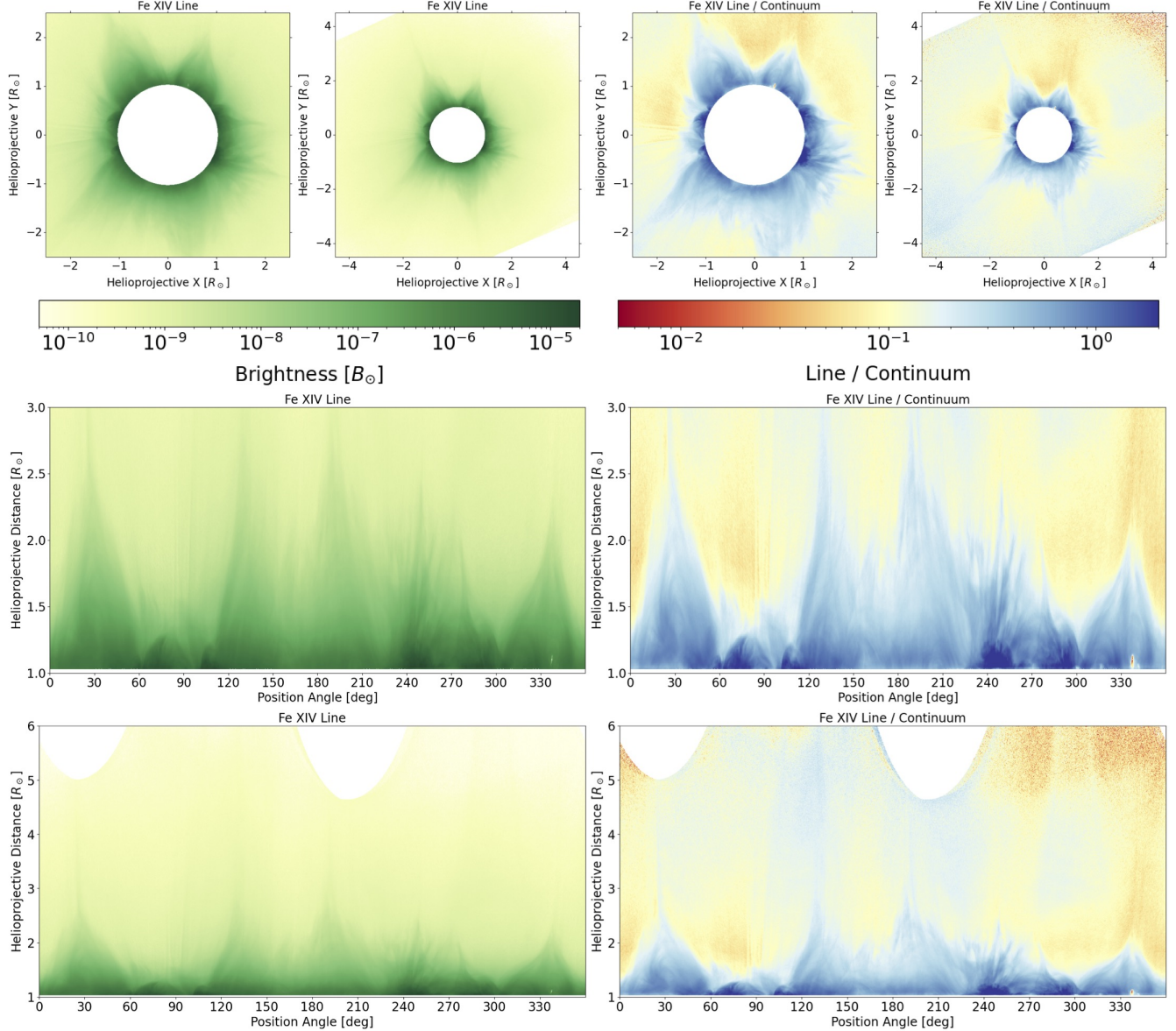


Figure 3. Emission of Fe XIV recorded with narrowband images (see Section 2.2). The panels on the left show the absolute line emission (in units of mean solar disk brightness) in log space, while the panels on the right show the line emission divided by the continuum (K+F corona) brightness near the same wavelength of the line. The top panels on each size show the corona with a window of $2.5 R_{\odot}$ (left) and $4.5 R_{\odot}$ (right) with Solar North upwards, while the bottom pairs of panels are in polar coordinates (Helioprojective distance vs Position Angle) extending out to 3 (top) and $6 R_{\odot}$ (bottom).

half maximum (FWHM) of approximately 1–1.5 nm (See Appendix A.2 for the exact bandpasses). For each emission line, we used two telescopes – one with a bandpass centered on top of the emission line, and a secondary one separated by ≈ 7 nm towards shorter wavelengths (i.e., blueward) than the emission lines. The secondary “Off-band” telescopes are essential since there is a strong continuum emission caused by scattering of photospheric light by electrons (K-corona; see P. Lamy et al. 2020) and dust throughout the solar system (F-corona; see H. Morgan & S. R. Habbal 2007). In fact, the K-corona

and F-corona have a brightness similar to the emission lines, even as low as about $1.3 R_{\odot}$, and are the dominant source of emission at visible wavelengths beyond $2 R_{\odot}$ at most (see Section 3.3).

Each narrowband telescope consisted of a 300mm Zeiss f/4 telephoto lens (7.5 cm aperture) with a narrowband filter on the front and a ZWO astrophotography camera on the back. For Fe X and Fe XIV we used the ZWO ASI1600MM camera (Panasonic MN34230ALJ sensor), which has a resolution of 4656×3520 pixels, with a pixel size of $3.8 \mu\text{m}$. For Fe XI we used the ASI294MM

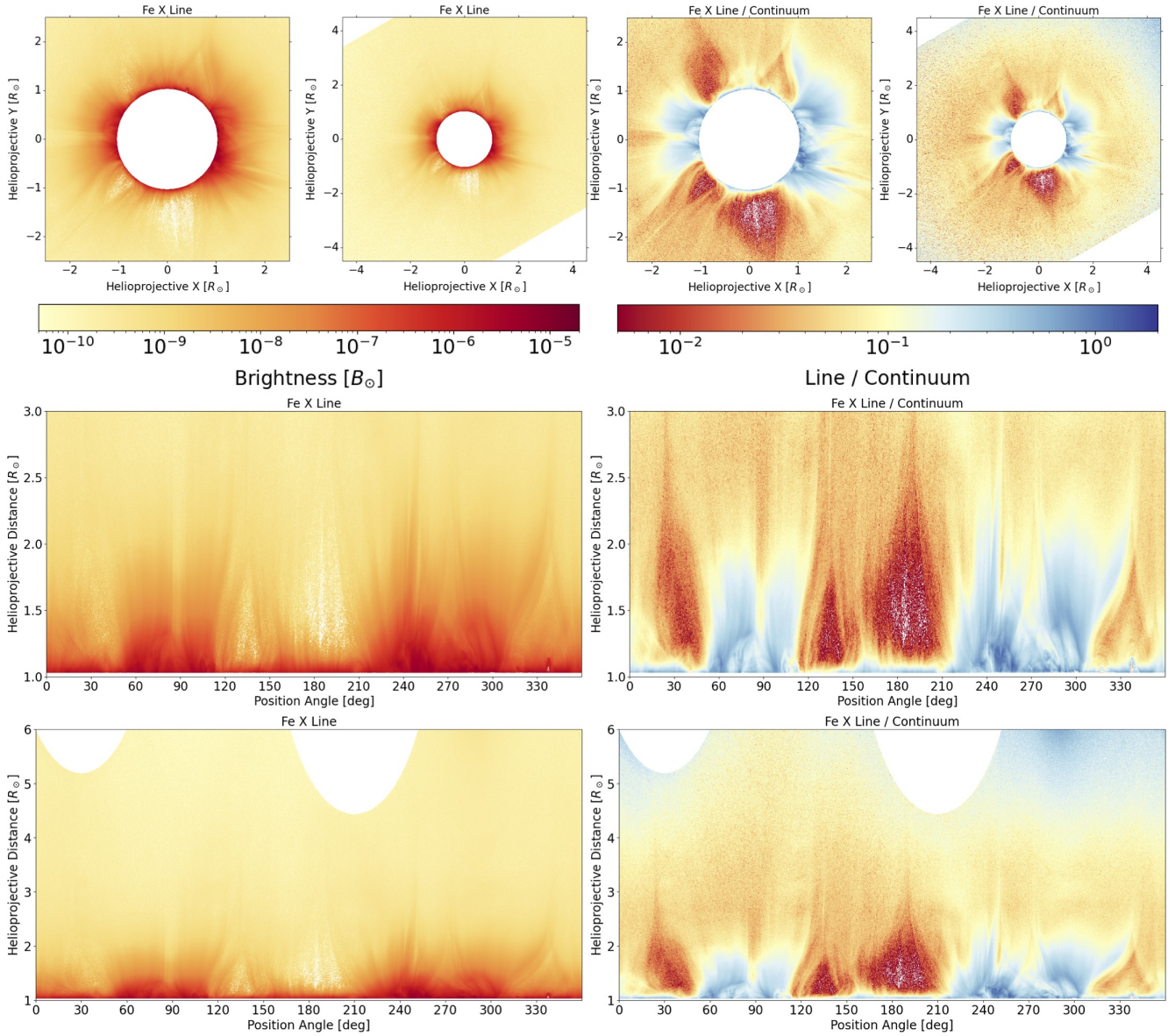


Figure 4. Same format as Figure 3 for Fe X emission.

camera (SONY IMX294 CMOS sensor), due to its higher sensitivity at infrared wavelengths. These cameras had a resolution of 8288x5644 pixels, with a pixel size of $2.3 \mu m$, which was re-binned into 2x2 pixels for a resolution of 4144x2822. Unfortunately, an unforeseen consequence of using the ASI294MM camera was that the back-illuminated chip design resulted in an Étalon-type interference pattern that caused some minor contamination of the Fe XI observations (only where the corona was very faint beyond about $3 R_{\odot}$). This issue did not appear during prior lab testing and is only visible with an extreme brightness contrast source such as that which occurs during a total solar eclipse.

All of the narrowband camera systems cycled through exposure times during totality, ranging from 0.025 s up

to 3.2 s, bracketed by factors of two for a total of 8 unique exposure times in the observing cycle. The sequence was then repeated throughout totality for a total of 32-35 usable exposures for each telescope system. Since totality was rather short, we opted not to do a simple exposure sequence in order, but rather had more of the shorter exposure times to coincide with the several seconds with the start and end of totality, and had additional longer exposures occur during the middle of totality. Optimizing the sequence in this way enabled more usable exposures without saturation contamination from the solar photosphere while also capturing as low down in the corona as possible during the shorter time that it was exposed.

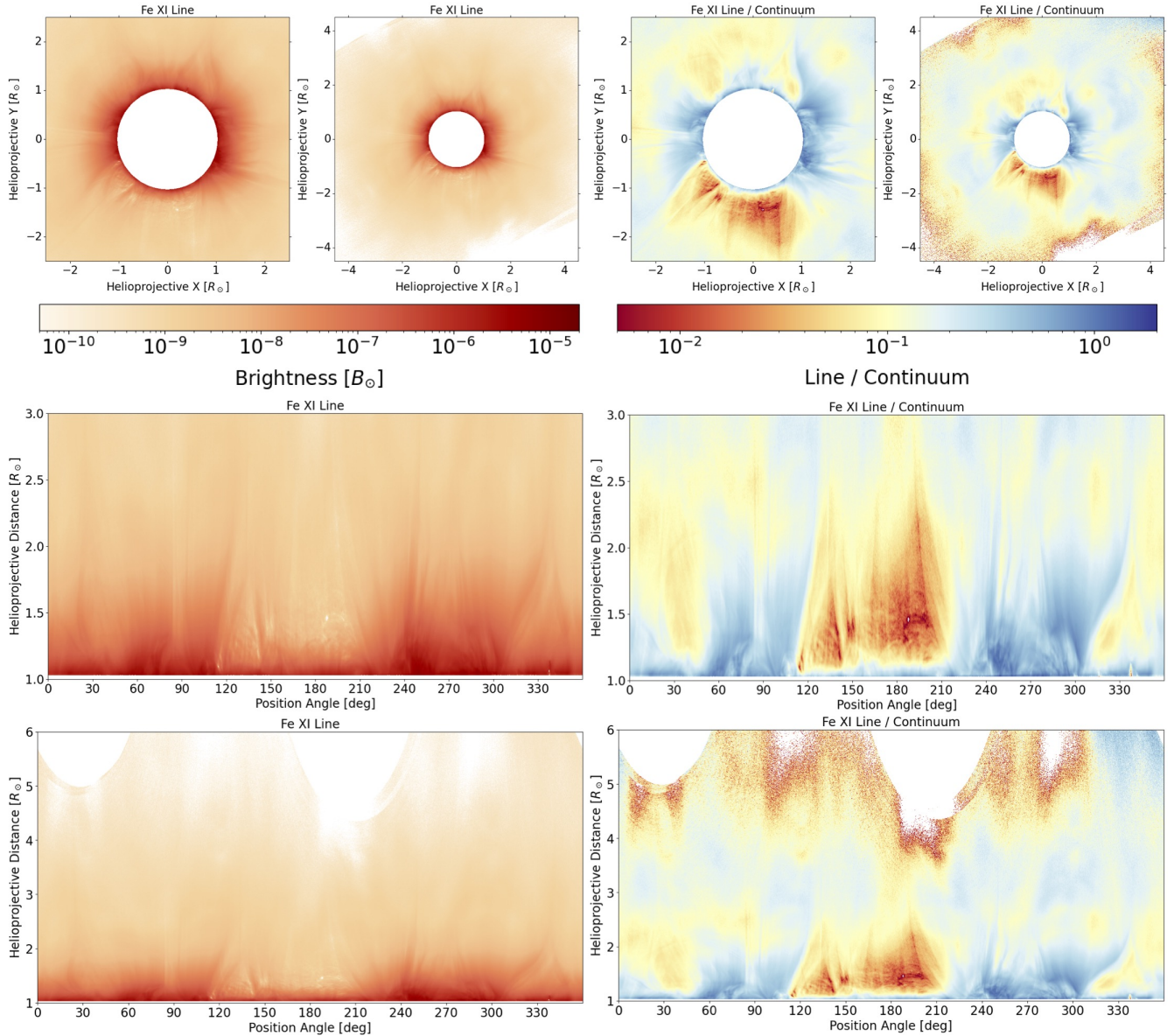


Figure 5. Same format as Figures 3 and 4 for Fe XI emission.

After the data reduction, all eclipse frames were co-aligned using a phase correlation method to account for the relative offset between each frame of the same telescope caused by the imperfect tracking by the mount. The data for each telescope were then stacked after accounting for the linearity of the cameras and photometrically calibrated using solar disk observations made after the eclipse (See Appendix A.3 for more details). Once each stacked observation was compiled, they were all co-aligned with each of the other observations (at both Exmouth and the Island), including the offset, rotation, and relative scaling of the images. Finally, the bright prominence in the North west part of the low corona was used to align the images with Solar North via the Global Oscillation Network Group (GONG) H- α data

(J. W. Harvey et al. 1996; F. Hill 2018). The continuum, as measured by each off-band dataset, was then subtracted from the on-band emission to isolate the line emission observation.

3. RESULTS

3.1. Line emission of Fe XIV, Fe X, and Fe XI

Upon completion of the reduction and processing described in Section 2 (and Appendix A), we produced observations of the emission from the Fe XIV, Fe X, and Fe XI lines from just above the solar surface (about $1.03 R_{\odot}$) outward to $6 R_{\odot}$, as shown in Figures 3, 4, and 5 respectively. Quantitative radial traces of the line emission are shown in Figure 6.

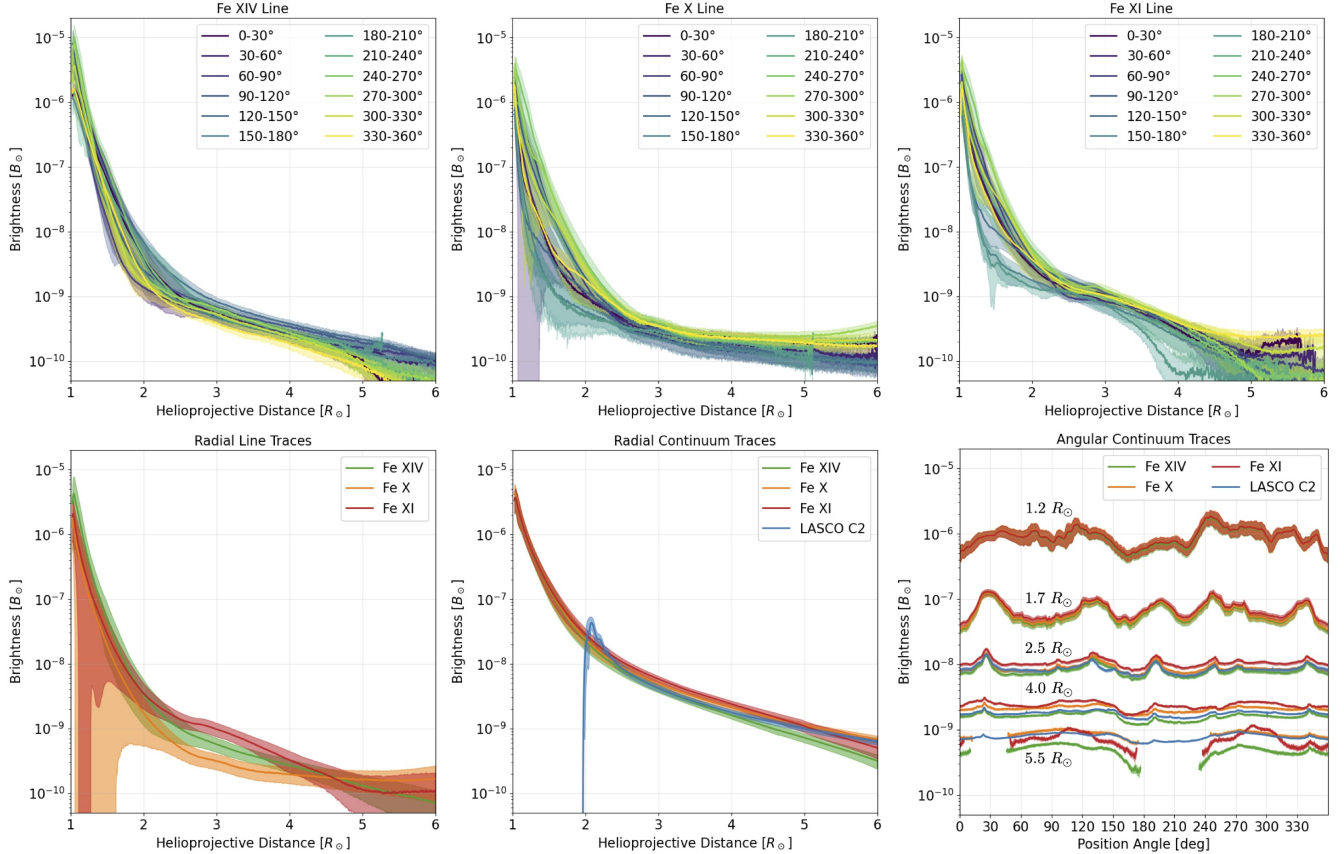


Figure 6. Quantitative traces of the observed line and continuum emission. The top panels show radial traces of the line brightnesses averaged over 30-degree position angle windows for Fe XIV (left), Fe X (middle), and Fe XI (right). The lines represent the median average, while the bands represent the standard deviation of the data in each region (which was always larger than the photometric error). The bottom left panel shows the brightness of all of the lines as a function of helioprojective distance, averaged over all position angles. The bottom middle panel is the same as the bottom left, but for the continuum observations corresponding to each line, as well as LASCO-C2. The bottom right panel shows position angle traces of those same continuum observations at a distance of 1.2, 1.7, 2.5, 4.0, and 5.5 R_{\odot} , averaged in a window of $\pm 0.05 R_{\odot}$ for each.

Due to the relatively different ionization equilibrium abundances as a function of the T_e , which are plotted in Figure 2, each of these emission lines originates from distinct structures along each LOS. Indeed, since the corona is optically thin, we expect to see a range of structures along the LOS with different T_e , which can be resolved by comparing the emission of these different ionic lines (e.g., E. Landi & M. Landini 1997; S. R. Habbal et al. 2010c; B. Boe et al. 2023a). The emission from each line can be thought of as a slice of the corona over the range of temperatures that the ion can exist, weighted by the density of the corona in those structures. Consequently, all of the lines fade dramatically with distance from the Sun as the density in the corona drops. Displaying the lines relative to the continuum (K+F corona) then offers a simple method to visualize the relative emission of the lines scaled by the background electron density. While this observable will be-

come biased by F-corona (dust) brightness farther out, it still enhances the visualization of the line.

For the Fe XIV line, which is weighted towards plasma from about 1.6 to 2.4 MK, the emission is brightest in closed field lines where the T_e is expected to be higher. In the data shown in Figure 3, the Fe XIV emission is significant out to a few solar radii in the streamer structures, and is very strong in smaller closed field lines near the equator (up to $2 \times 10^{-5} B_{\odot}$). Once the coronal field becomes more open, the Fe XIV emission drops significantly. In the low closed structures, the line emission is comparable to or even a few times brighter than the background continuum, but it quickly drops to about 10% of the continuum brightness farther out in the corona. However, the line emission then plateaus and remains around 15-20% of the continuum brightness outward to 6 R_{\odot} .

In contrast to the Fe XIV line, the Fe X line is weighted towards cooler plasma from about 0.7 to 1.4 MK. Hence,

the Fe X line originates primarily from open-field regions such as coronal holes. In Figure 4, the Fe X emission is brightest in the open-field corridors seen near the equator of the Sun (around 50-110 and 220-310 PA) with values of a few times $10^{-6} B_{\odot}$. On the other hand, the Fe X emission is extremely faint in the hotter closed field regions near the solar poles. In fact, the southern streamers (from about 115-215 PA) have a nearly undetectable amount of Fe X emission, particularly at a distance of 1.2 to 2 R_{\odot} . The Fe X emission is likely still present in those streamers, but the SNR is simply too low to extract it from the background continuum signal in our dataset. Once the continuum brightness drops, the Fe X emission returns and is seen across all position angles out to 6 R_{\odot} , with values around a few times $10^{-10} B_{\odot}$. The Fe X brightness has a similar relationship to the continuum as does Fe XIV, with the brighter regions getting close to the same brightness as the continuum, but then dropping to about 10 % of the continuum brightness.

The Fe XI emission, which is weighted towards plasma from about 1.0 to 1.8 MK, unsurprisingly shows a similar behavior to Fe X. The slightly higher temperature response of Fe XI does lead to the line being stronger in the southern streamers, though it too has a few points where the emission is not detectable above the SNR. However, the Fe XI shows a lot of fine-scale structures throughout the streamers as well as in the open-field corridors. In contrast with the other two lines, it provides an intermediate scan of coronal temperatures.

Unfortunately, the detectors for Fe XI had an Étalon-type interference issue originating from the back-illuminated detector (and near-infrared wavelength) which contributed some contamination of the emission beyond around 2.5-3 R_{\odot} . While the contamination blurs the exact spatial behavior of the emission, it is still apparent that the line is strong out to at least 4 R_{\odot} with likely detections out to 6 R_{\odot} (albeit with a lower confidence than Fe X and Fe XIV). In fact, around 2.5 to 4.5 R_{\odot} , the Fe XI line is the brightest of the three lines.

Despite the spatial variance across unique fine-scale structures, all three lines show a similar behavior with distance. These lines are strong low down in the corona (at least $4 \times 10^{-6} B_{\odot}$, with Fe XIV up to $2 \times 10^{-5} B_{\odot}$) and fade to about $1 - 5 \times 10^{-10} B_{\odot}$ at 6 R_{\odot} for all position angles. All of the lines also show a rapid decrease in brightness between 1 and about 2 – 2.2 R_{\odot} , then the slope of the brightness drop bends to be much less steep beyond that distance (see Figure 6). These kinks in the emission profiles are likely caused by the transition from the lower part of the corona, where collisional excitation of the lines is common, to the outer corona,

where collisions fade and radiative excitation becomes the dominant line formation mechanism (see S. R. Habbal et al. 2007; D. B. Seaton et al. 2021; B. Boe et al. 2023a).

3.2. Line Emission Ratios

As discussed earlier in Section 3.1, the exact brightness of each emission line depends on the density and T_e of each structure. Thus, the relative emission of the lines can be used as a probe of the physical state of the corona. All lines show a similar trend in the structure of the line emission with helioprojective distance, which is caused by the steep drop-off in coronal density. To highlight the differences in the T_e of various coronal structures, we took the ratio of each line to every other line (which largely corrects for the overall density).

The line emission ratios of Fe X/Fe XIV, Fe XI/Fe XIV, and Fe X/Fe XI, are all shown in Figure 7 in the top, middle and bottom rows respectively. The left column shows these ratios out to 2.5 R_{\odot} , showcasing the variability of the T_e of structures in the lower corona. The middle column shows the ratios out to 4.5 R_{\odot} , and the right column shows the ratios in polar coordinates, which probes the T_e structures out to 6 R_{\odot} .

It is important to note that these line ratios really represent the emissivity-weighted LOS T_e distribution. While they do not provide an exact T_e for a specific chunk of coronal plasma, they do represent a physically interesting value illustrating the temperature structure of the corona. The combination of all three lines could then be used to infer the T_e distribution along each LOS, after accounting for the excitation mechanisms of each line. This sort of inference is referred to as a Differential Emission Measure (DEM, see G. Del Zanna & H. E. Mason 2018), though DEMs have typically been done with collisionally excited EUV and X-ray lines. A Radiative version of a DEM (RDEM) was introduced by B. Boe et al. (2023a) and applied to these same three emission lines using data from the 2019 TSE, leveraging a 3-dimensional (3D) global Magnetohydrodynamic (MHD) simulation to account for the relative amount of collisional and radiative excitation. We also intend to produce such inferences with these data, including a 3D MHD model to estimate collisional excitation of the lines. Yet, the MHD simulation would itself warrant significant analysis, discussion, and comparison to other observational datasets. Therefore, a full RDEM inference is beyond the scope of this initial instrumentation, calibration, and observation paper. Here, we will discuss the initial findings from these line ratios.

Based on the emission line ratios, the corona is divided into two main structures: a few large higher-

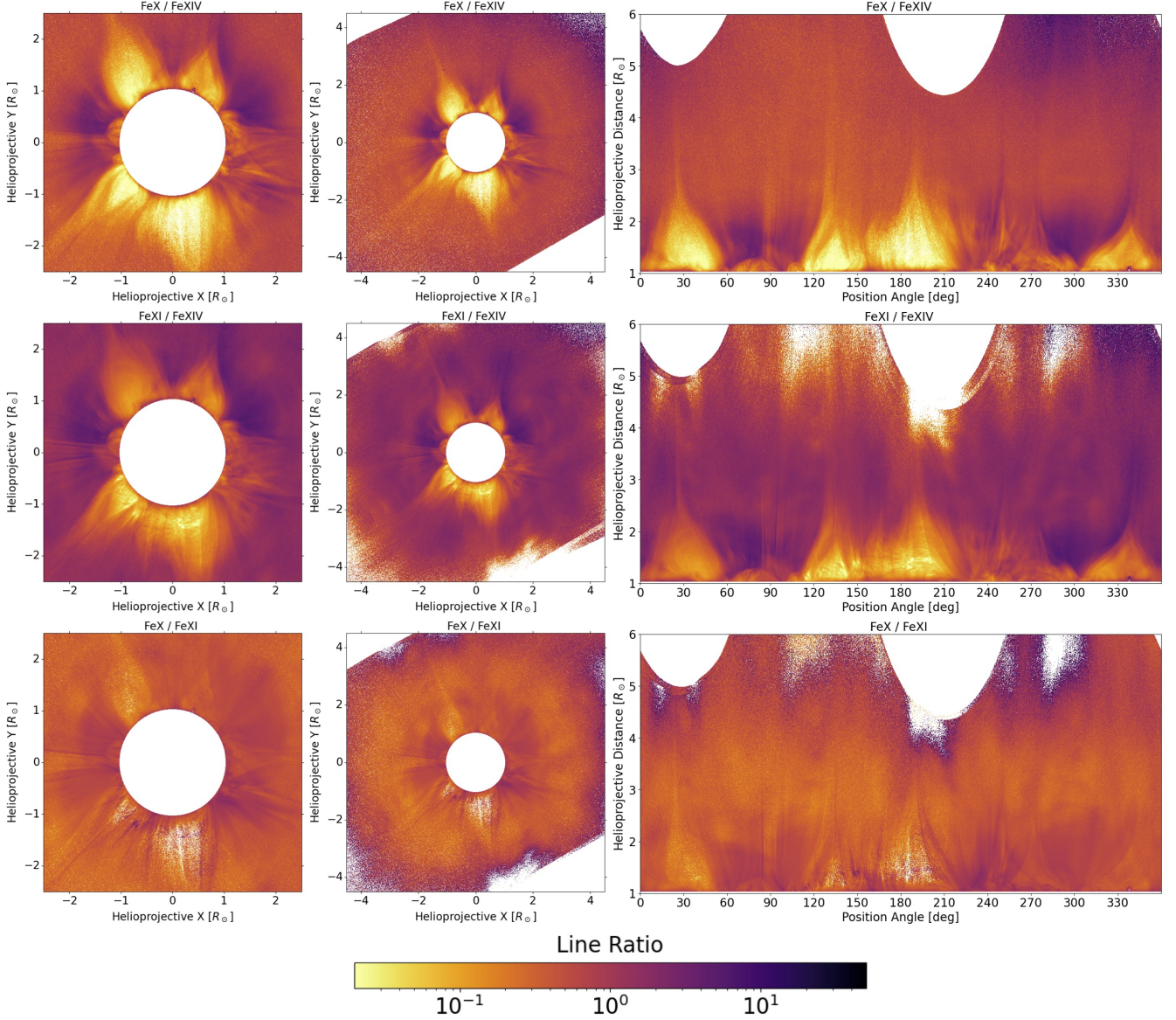


Figure 7. Collection of line emission ratios of Fe X / Fe XIV (top row), Fe XI / Fe XIV (middle row), and Fe X / Fe XI (bottom row). The emission ratios are shown out to $2.5 R_{\odot}$ in the left panels and $4.5 R_{\odot}$ in the middle panels, and in polar coordinates out to $6 R_{\odot}$ in the right panels.

temperature polar streamers and two large lower-temperature equatorial open-field regions. The highest temperature regions of the corona during this eclipse are clearly the two southern streamer arcades between about 120 and 215 PA. Inside these streamers, Fe XIV emission dominates, while the Fe X emission drops below the detection threshold in the streamer cores. The Fe XIV/Fe XI line ratio highlights how those streamers have by far the largest relative amount of Fe XIV emission, indicating a T_e of approximately 1.7-2 MK or more.

The streamers to the northeast (about 0 to 60 PA) and the northwest (300 to 360 PA) have considerably more Fe XI and Fe X emission relative to Fe XIV, indi-

cating a more moderate average temperature closer to 1.5 MK. It is interesting that the northwest streamer, which has a large prominence, actually is much brighter in Fe X emission compared to the other large streamers, suggesting a lower average T_e . However, there is a large open-field plume that is pushing on the streamer from the south (around 320 PA), which could be overlapping along the LOS and biasing the ratio towards the cooler ions.

The other primary structures are two large open-field regions on the solar equator (at around 35-125 and 270-320 PA). These open-field corridors show a much larger amount of Fe X and Fe XI emission, suggesting a lower

temperature around 1.1-1.4 MK. The Fe X/Fe XI ratio is weighted towards these cooler open-field lines, and so can resolve fine-scale plumes inside the open-field regions while not highlighting the higher T_e streamers. The open-field corridors show a strong expansion with helioprojective height, as opposed to the streamers, which pinch off into narrow streamer stalks. The tips of these streamer stalks can be seen in some cases out to $6 R_\odot$ in the line Fe XIV/Fe X ratio.

These line ratios also change with helioprojective height throughout the corona, particularly showing more Fe X and Fe XI emission (below $1.3 R_\odot$) compared to Fe XIV even at the base of hot streamers, but then an increasing amount of Fe XIV beyond at larger heights. This finding was seen with these same lines for the 2019 eclipse (B. Boe et al. 2023a) and might be an indication that heating is occurring low down in the corona, or perhaps could be an effect related to the temperature dependence of the scale height (see M. J. Aschwanden & N. Nitta 2000).

There is also an intricate structure around 215 to 290 position angle that is not easy to define cleanly as either an open-field region or a streamer. It could be a mix of both based on the fact that it shows the brightest emission from all three lines. There was a similar report by B. Boe et al. (2020), who found that above an active region on the limb during the 2017 TSE had strong emission from Fe XI and Fe XIV.

Below about 2.5 to $3 R_\odot$, these line ratios (as well as the line emission itself) show a large amount of structural variation along the POS. That is, there is a preponderance of small-scale structures with unique temperatures. However, beyond $3 R_\odot$, the corona becomes increasingly flat regardless of the underlying structure. The Fe XI emission (and ratios including it), unfortunately suffered from the Étalon-type interference issue (see Section 2.2), which limits their substantive analysis beyond $4 R_\odot$. Still, the Fe XIV/Fe X ratio becomes exceptionally flat throughout the corona, besides a few streamer stalks. This finding indicates that most of the corona is becoming nearly isothermal beyond $3 R_\odot$, which is consistent with work from prior eclipses as well as in situ data on the ionic abundances in the solar wind, independent of the solar cycle (S. R. Habbal et al. 2010b, 2021).

Nevertheless, there is an interesting feature around a PA of 270 to 330 degrees, where the Fe X emission rises and the Fe XIV emission fades. The resulting line ratio indicates a significant deviation from the rest of the corona. This region corresponds to a location directly above a large open-field corridor that has strong Fe X emission lower down in the corona. It is plausible that

this increase is due to time-dependent release of cooler material from that open-field region (or a tiny CME), perhaps through some sort of interchange reconnection with the streamers on either side. However, it is difficult to make any strong claims about this finding given the low SNR of the emission in that region.

3.3. Continuum Observations

The continuum observations from all off-band narrow-band observations (see Section 2), as well as the LASCO-C2 observations at the exact same time as totality in Exmouth (03:30 UT), are shown in Figure 8. Quantitative traces of the continuum data are shown in Figure 6, where the bottom middle panel contains traces as a function of helioprojective distance and the bottom right panel has traces at fixed heights of 1.2, 1.7, 2.5, 4.0, and $5.5 R_\odot$ (each averaged over $\pm 0.05 R_\odot$) for all position angles.

The continuum observations show the combination of both the K-corona (electron scattering) and F-corona (dust scattering). As discussed in Sections 1 and 2, the F-corona has a color relative to the solar spectrum, where it is brighter at redder wavelengths. This color effect necessitates the deployment of off-band telescopes with narrowband filters near each line. These observations can then provide information on the K and F corona via their relative brightness.

The continuum data for the Fe X off-band (at 630.4 nm, see Appendix A.2) are used as the primary reference for the absolute calibration of all the imaging data (using solar disk observations, see Appendix A.3). However, the Fe XIV continuum has the lowest F-corona contribution, so it is the best approximation of the K-corona. The Fe XIV continuum data are shown out to 2.5 and 4.5 in the top left two panels of Figure 8. The Fe X continuum is the closest in wavelength to the LASCO-C2 Orange filter (see P. Lamy et al. 2020), so we compare the Fe X continuum and LASCO-C2 observations with the same perspective of $6 R_\odot$ in the top right panels. The Fe XIV continuum is then shown in polar coordinates in the middle-left panel. The ratio of the brightness of LASCO-C2 and the Fe X continuum, as well as the Fe X and Fe XI continua relative to the Fe XIV continuum, are shown in the middle-right, bottom-left, and bottom-right panels, respectively.

The overall structure of the continuum is rather simple, with the streamers at the north and south having the largest brightness and extending outward with stalks going out to at least $6 R_\odot$. The regions identified as cooler open-field corridors in Section 3.2 do have a lower continuum brightness, but they are not nearly as easy to distinguish as they were with the line emission

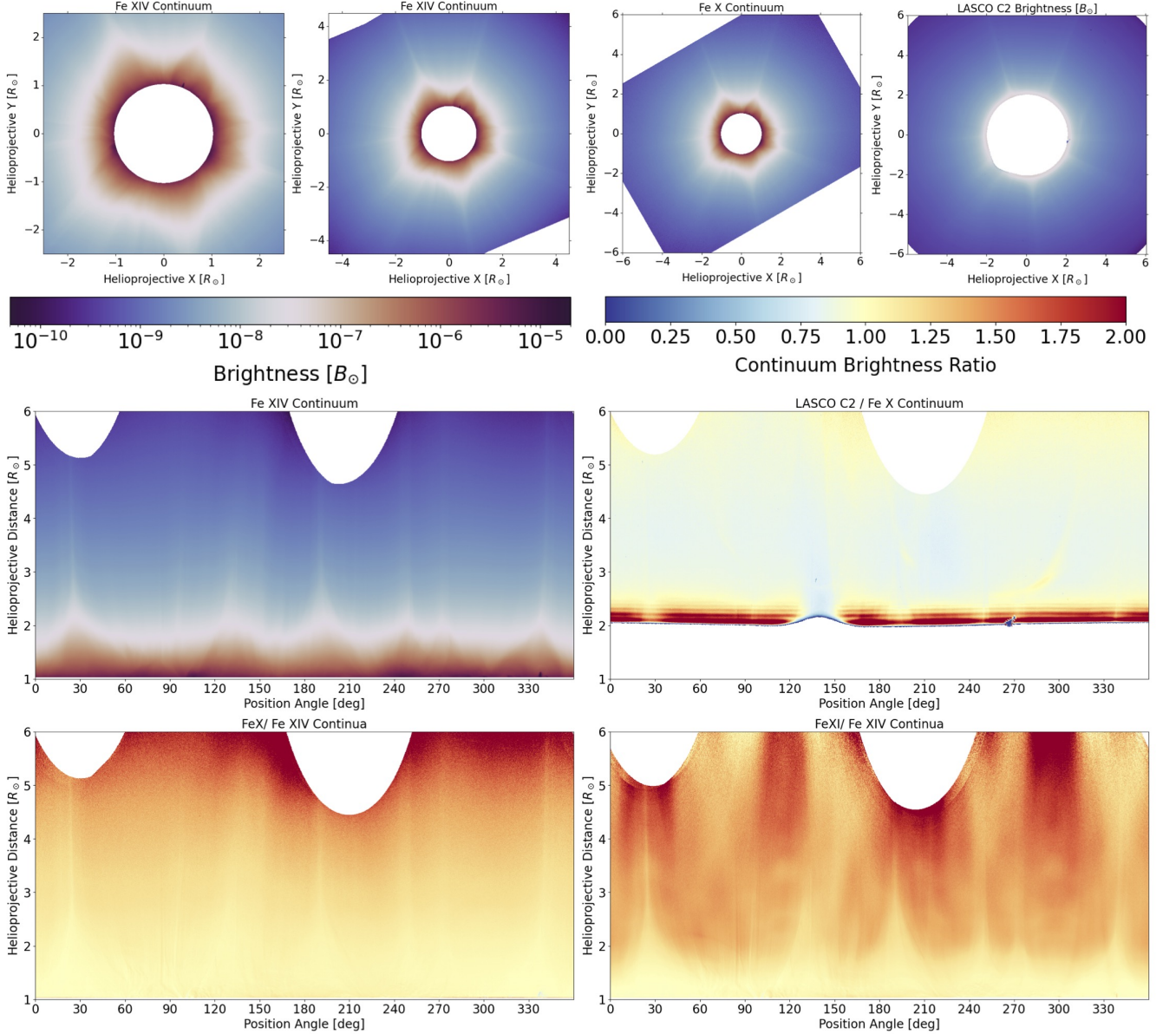


Figure 8. Observations of the continuum emission during the eclipse (see Section 3.3). The top row shows the continuum near the Fe XIV line out to 2.5 (left) and 4.5 (middle-left), the Fe X continuum out to $6 R_{\odot}$ (middle-right) as well as the LASCO-C2 emission out to $6 R_{\odot}$ (right). The bottom panels then show the Fe XIV continuum in polar coordinates out to $6 R_{\odot}$ (top left), as well as continua ratios of LASCO-C2/Fe X (top right), Fe X/Fe XIV (bottom left), and Fe XI/Fe XIV (bottom right)

data. In general, this corona near solar maximum has a remarkably small variation in continuum brightness at any given helioprojective distance, other than the small streamer stalks and small closed field regions low down (below about $1.5 R_{\odot}$).

Farther out in the corona (beyond $2 R_{\odot}$), the observed LASCO-C2 emission is quite consistent with our Fe X continuum. These LASCO-C2 data were taken from

the Legacy Archive⁵, which provides processed data accounting for stray light, vignetting, cosmic rays, orientation of the spacecraft, and a photometric calibration from standard stars (A. Llebaria et al. 2012; P. Lamy et al. 2014; E. Pagot et al. 2014; P. Lamy et al. 2020).

The independent comparison to LASCO-C2 validates our photometric calibration, matching exactly at a height of about $2.5 R_{\odot}$. The LASCO-C2 brightness is

⁵ <http://idoc-lasco.ias.u-psud.fr/sitools/client-portal/doc/>

considerably higher below $2.5 R_{\odot}$ (above the occulter), likely indicating the presence of additional light from the solar disk that has diffracted around the occulter. There are also a few streaks of stray light present around 70, 190, and 250-320 PA at distances of roughly 2.8 - $4.5 R_{\odot}$.

The brightness of the LASCO-C2 brightness falls after $2.5 R_{\odot}$, relative to our continuum observation. It then becomes closer to our data again, beyond about $5 R_{\odot}$. This behavior hints at a slightly inaccurate accounting of the LASCO-C2 vignetting profile as a function of height. Further, the occulter arm, at about 130-150 PA, shows the lowest relative continuum brightness, strongly indicating that the attenuation caused by the blocking arm is not perfectly accounted for. Nevertheless, the LASCO-C2 and eclipse continuum agree to within 10-20% throughout the entire corona, other than near the occulter and the occulter arm. This comparison highlights the exceptional accuracy that has been achieved with the LASCO-C2 processing and showcases how valuable eclipse data are for validating coronal observations by coronagraphs and vice versa.

The continuum observations for the FeX and FeXI lines are shown as a ratio to the FeXIV continuum in the bottom panels of Figure 8. As previously demonstrated by B. Boe et al. (2021), the F-corona has a color effect where it becomes brighter at longer wavelengths. This effect causes the FeX continuum to slowly rise relative to FeXIV continuum, becoming more than 50% at about 4.5 - $5 R_{\odot}$. The FeXI continuum shows an even more dramatic effect, becoming 50% brighter than the FeXIV continuum as low as $1.5 R_{\odot}$. Still, all continua observations agree below about $1.3 R_{\odot}$.

The combination of these continuum data can be used to extract the relative K- and F-corona signals, but to do so robustly requires an accounting of the slight color that the K-corona has due to limb-darkening. Limb-darkening changes at different wavelengths, which in turn changes the angle-dependent incident radiation that changes the K-corona brightness (also depending on the 3D density structure of the corona). The best way to account for this effect is with a global 3D MHD model, which we intend to do in the future. Ergo, we defer that more detailed analysis to a subsequent study.

4. DISCUSSION AND CONCLUSIONS

In this work, we presented observations from the 2023 TSE in Australia, including high-resolution white-light data (see Section 2.1) and narrowband emission observations of the ionic emission lines of FeXIV, FeX, and FeXI (see Section 2.2). The narrowband data were carefully processed and calibrated to the solar disk (see Appendix A). The narrowband continuum observations (see Sec-

tion 3.3), which were used to remove the background K- and F-corona continuum emission, were then validated against LASCO-C2 observations at the same time, demonstrating the reliability of our telescopic systems. The primary result of this work is the demonstration that visible and near-infrared line emission can be observed throughout the solar corona from just above the photosphere ($1.03 R_{\odot}$) out to at least $6 R_{\odot}$ (see Section 3.1).

Additionally, these observations are possible with less than a single minute of exposure time, in contrast to prior observations of ionic line emission in the UV beyond $4 R_{\odot}$, which have typically required long exposure times of 10 minutes or even hours of co-added exposures to get reasonable SNR at these distances (e.g., L. Zangrilli & G. Poletto 2012; S. Giordano et al. 2013; F. Auchère et al. 2023). The main benefit to observing emission lines at visible and infrared wavelengths (and near-UV) is their ubiquitous excitation by photospheric light, hence they are an important tool for probing the corona beyond 1.5 - $2.5 R_{\odot}$.

The nature of the line emission itself showcased some notable features of the corona during the eclipse, near the maximum of the solar activity cycle. Low down in the corona, there are a multitude of fine-scale structures seen both in the white-light image as well as in the structure of the line emission. There are plumes of open field lines emitting more FeX in contrast to multiple streamers that emitted much more FeXIV due to their higher T_e . The average T_e can be qualitatively inferred from the line ratios (see Section 3.2 and Figure 7), which indicate that throughout the streamers and open field corridors, there was a large amount of spatial variation of the ionic lines, indicating variability in the density and temperature of the coronal structures.

On the other hand, beyond about $3 R_{\odot}$, the corona appears to become remarkably isothermal, with a nearly flat FeX/FeXIV line emission ratio throughout the corona. This behavior of a nearly isothermal distribution of temperature beyond about 2 - $3 R_{\odot}$ has been seen commonly before during eclipse observations (S. R. Habbal et al. 2021), including during solar minimum (B. Boe et al. 2023a), and based on the frozen ionic charge states seen in situ (S. R. Habbal et al. 2010b). This study further supports the consistency of these findings, even during solar maximum. It is important to note that the ions may be frozen-in by $3 R_{\odot}$ (e.g., see B. Boe et al. 2018), meaning that the “isothermal” temperature may apply not at $3 R_{\odot}$ in particular, but rather to the freezing-in point of the majority of solar wind sources – which is still a physically insightful finding for models to benchmark against.

The large array of valuable physical inferences that are possible with visible and infrared coronal line emission (see Section 1), combined with the proven spatial extent of these radiatively excited emission lines at visible and infrared wavelengths out to at least $6 R_{\odot}$, as demonstrated in this work, emphasizes the importance of observing these lines farther out in the corona. In particular, it supports the necessity of future eclipse observations and the development of ground- and space-based coronagraphs to observe these lines. There are a number of ground- and space-based observatories recently coming into operation (or soon to be), yet none of them are capable of probing more than one of these lines throughout the middle corona.

On the ground, all observations are currently limited in helioprojective extent below about 1.5 to $2 R_{\odot}$ due to stray light and atmospheric brightness on the Earth. In particular, the Coronal Multi-channel Polarimeter (CoMP; S. Tomczyk et al. 2008) established routine observations of Fe XIII 1074.7 nm and is now being replaced by an upgraded COMP (UCoMP; S. Tomczyk et al. 2022⁶). There have also been new high-spatial/spectropolarimetric resolution observations by the Daniel K. Inouye Solar Telescope (DKIST; T. R. Rimmele et al. 2020). However, at present, DKIST can only observe the density-sensitive Fe XIII line pair (1074.7 nm and 1079.8 nm) along with Si X 1430 nm line over a very small field-of-view (T. A. Schad et al. 2024b), which does limit its current capabilities for probing the T_e distribution in the corona.

In space, there are new observations from Metis and from ASPIICS on PROBA-3 (D. Galano et al. 2018; A. N. Zhukov et al. 2025) which will be able to probe the region between ≈ 1.1 and $4 R_{\odot}$ (depending on orbital distance for each spacecraft). However, they will collectively only have filters for He II 30.4 nm, H I 121.6 nm, He I 587.7 nm, and Fe XIV 530.3 nm. The one Fe XIV line from ASPIICS will be a useful dataset for demonstrating time variability of the line, and for comparison to eclipse data, but it will be unable to measure the coronal T_e on its own without another ionic line. Indeed, other than Fe XIV with ASPIICS and VELC, no visible or infrared coronal emission line has been observed in space since the untimely failure of the LASCO-C1 instrument in 1998 (see Section 1).

Given the clear importance of these visible and infrared emission lines for better characterizing the physics of the solar corona beyond $2 R_{\odot}$, which is crucial for investigating the connection between the corona and so-

lar wind, there is a strong need for a new generation of spacecraft that can observe several of these lines to large helioprojective distances (see the Decadal Survey White Paper by B. Boe et al. 2023b). Occultation of the photosphere could be accomplished with a traditional coronagraph, a secondary spacecraft (recently proven by ASPIICS; A. N. Zhukov et al. 2025), or even using the Moon from a lunar orbit (S. R. Habbal et al. 2013; J. F. Cooper et al. 2023). Additionally, recent airborne TSE observations by J. E. Samra et al. (2022a,b, 2025) have demonstrated that there are several emission lines farther in the infrared that could be used as well, further justifying the need for spectroscopic observations (via narrowband filters and/or spectrometers) spanning the visible and infrared spectrum.

Just as observations of ionic emission at visible wavelengths launched the field of coronal physics over a hundred and fifty years ago, so too are these lines important for pushing the field forward now. They offer an important alternative that has distinctly different advantages and drawbacks compared to lines in the EUV and other wavelengths. A new generation of observatories, with complementary data spanning the entire wavelength range of corona emission, including X-rays, EUV, near-UV, visible, infrared, and radio (which provides important constraints on the magnetic field; see D. E. Gary et al. 2013; D. E. Gary 2023), should be developed and deployed. Each of these wavelength bands offers unique information on the physics of the corona, and equipped with high-quality data from all of them simultaneously, we would likely be able to significantly advance coronal physics beyond what is possible with any one set of wavelengths alone.

ACKNOWLEDGMENTS

We thank Adalbert Ding and Judd Johnson for their work developing earlier generations of narrowband instrumentation that led to these new instruments, as well as for their input and advice on the 2023 eclipse expedition.

The eclipse expedition was supported by NSF grant AGS 21303171 (PI was SH). BB was supported by NSF SHINE grant AGS 2501212. This publication was supported by the project “Innovative Technologies for Smart Low Emission Mobilities”, funded as project No. CZ.02.01.01/00/23_020/0008528 by Programme Johannes Amos Comenius, call Intersectoral cooperation. SC was supported by a DKIST Ambassador fellowship (AURA N00032456C).

This work makes use of the LASCO-C2 legacy archive data produced by the LASCO-C2 team at the Lab-

⁶ <https://www2.hao.ucar.edu/mlso/instruments/upgraded-coronal-multi-channel-polarimeter>

oratoire d’Astrophysique de Marseille and the Laboratoire Atmosphères, Milieux, Observations Spatiales, both funded by the Centre National d’Etudes Spatiales (CNES). LASCO was built by a consortium of the Naval Research Laboratory, USA, the Laboratoire d’Astrophysique de Marseille (formerly Laboratoire d’Astronomie Spatiale), France, the Max-Planck-Institut für Sonnensystemforschung (formerly Max Planck Institute für Aeronomie), Germany, and the School of Physics and Astronomy, University of Birmingham, UK. SOHO is a project of international cooperation between ESA and NASA.

This work utilizes GONG data obtained by the NSO Integrated Synoptic Program, managed by the National Solar Observatory, which is operated by the Association of Universities for Research in Astronomy (AURA), Inc. under a cooperative agreement with the National Science Foundation and with contribution from the National Oceanic and Atmospheric Administration. The GONG network of instruments is hosted by the Big Bear Solar Observatory, High Altitude Observatory, Learmonth Solar Observatory, Udaipur Solar Observatory, Instituto de Astrofísica de Canarias, and Cerro Tololo Interamerican Observatory.

AUTHOR CONTRIBUTIONS

BB was the primary author of the paper and led the work to reduce, calibrate, and analyze the narrowband

data. BB also directed the narrowband observations on-site in Exmouth, including operating the narrowband imaging mount during totality. SH led the overall eclipse expedition and contributed significantly to the writing of the paper. MD processed the broadband white-light data and made the narrowband composite image in Figure 1. MD also contributed significantly to the planning of the expedition. PS and MS were the primary designers and manufacturers of both the physical and software infrastructure to operate the instrumentation. PS operated the white-light and slit-less flash spectrum instrumentation during totality. MS and JH were the sole operators at the secondary Island site. EA, SC, and DC all contributed to the preparations in Exmouth, including transport and assembly of the equipment, and collection of both eclipse and calibration data. Contributions to the 3D printing of components was made by PS, MS, EA, and SC. SC assisted BB after the expedition in collecting lab calibration data.

Facilities: GONG, SOHO/LASCO-C2

APPENDIX

A. INSTRUMENT CHARACTERIZATION AND CALIBRATION

This appendix contains an overview of details pertaining to the operation, collection, and analysis of the narrowband data from the 2023 April 20 TSE. The primary information about the expedition and types of data collected was described in Section 2. On site in Exmouth, we had a complement of several individual telescopes to collect emission from the Fe XIV, Fe X, and Fe XI emission lines and nearby coronal continuum. We then had a secondary site on an Island off the coast of Australia that had only Fe XIV and Fe XI imaging systems.

A.1. Instrumentation

A picture of the observing setup in Exmouth is shown in panel A of Figure A1. In order to maximize the number of telescopes per mount, we used a machined aluminum infrastructure to hold up to eight telescopes in a grid, with an additional slit-less spectrum camera mounted on the side (see on the lower left of the

mount in the image). The Sky-Watcher EQ6 mount was pushed to the absolute weight limit with this setup, so we fashioned custom counter-weights constructed with PVC pipes filled with locally-sourced (and returned) rocks. For the mobile site on the Island, we used smaller Sky-Watcher EQ5 mounts that had only two telescopes per mount.

Each telescope was held within the aluminum array using 3D printed plastic holders that had adjustable tip/tilt screws to co-align the systems, as well as to adjust and lock the lens focus. Both the alignment and focus were optimized by observing the solar disk with all systems, using additional mylar filters to protect the instruments from the high intensity of the photosphere (equipped on the cameras in the image in Figure A1). The tip/tilt was set by centering the Sun in the field-of-view (FOV) of all cameras simultaneously, while the focus was refined using software that measured the exact size of the solar disk as a function of the focus setting, which allowed nearly diffraction-limited focus for all systems. Each pair of cameras (i.e., each on/off-bandset for

each line) was then operated by a single laptop. Using the same laptop enabled us to synchronize the times of exposure for each pair of on/off observations for the same line. In the event of light cloud cover, we planned to use the synchronization as a way to remove the effect of the cloud attenuation in each exposure, but that was not required since both observing sites had fantastic conditions during totality.

After all the eclipse data had been co-aligned, we determined the correct orientation of the images (to have solar north upward) using H- α observations made by the GONG observatory at the Udaipur station in India (J. W. Harvey et al. 1996; F. Hill 2018). We averaged all of the H- α data taken within a window of ± 15 minutes of the time of totality in Exmouth, resulting in the data shown in panel B of Figure A1. Coincidentally, the Learmonth, Australia GONG station was less than forty kilometers away from our observing site in Exmouth, but since they experienced totality as well, the data from Udaipur were better for this alignment purpose. There was a rather large prominence in the northwest part of the solar disk, which was used to get a strong phase correlation match between the eclipse data (which also had that prominence) and the GONG data.

A.2. Narrowband Filters

As discussed in Section 2, each emission line requires both an on-band observation centered on the line emission and a second off-band observation to quantify the nearby continuum. The exact filters used in this work are shown in the middle column of Figure A1 for Fe XIV (top), Fe X (middle), and Fe XI (bottom). The widths of these bandpasses were increased to about 1-1.5 nm FWHM, in contrast to our earlier systems, which used 0.5 nm FWHM filters. The primary reason for the larger width is due to the expected increase in coronal line-widths as a function of height (e.g., R. Esser et al. 1999; B. Boe et al. 2022), so these wider filters are able to more accurately measure the brightness of the lines to large helioprojective distances. One additional advantage of the larger filter widths is that they do not require a heater assembly to ensure a precise temperature, while the older filters did due to their stronger sensitivity to temperature dependency in their transmission spectrum. The separation of several nanometers for the off-band filters was also essential, as prior observations with smaller separations of only 0.9-1.4 nm found Doppler shifted emission in the Off-band observations from a halo-CME (B. Boe et al. 2020). The 7 nm separation is more than sufficient to ensure there will not be any possibility of Doppler shifted contami-

nation (would require velocities >2000 km/s) while also remaining close enough in wavelength to prevent any F-corona related color effects on the background continuum.

The reason we observed these three coronal lines in particular was due to their consistently being the brightest coronal lines in the visible and near-infrared (below 1000 nm), but also due to their response to electron temperature. The ionization equilibrium abundance of these three ions as a function of electron temperature (see Figure 2). These ions probe the majority of coronal plasma from 0.8 to 2.4 MK, which contains almost all regions in the corona other than the cores of high-temperature active regions and flares (see B. Boe et al. 2023a). Thus, probing the emission of each of these lines enables an inference of the approximate coronal T_e resolved for different structures in the corona.

A.3. Calibration

To photometrically calibrate the data, we used observations of the solar disk taken after totality. In particular, we took observations with the Fe X off-band system with additional neutral density (ND) filters that had a net attenuation of 2×10^{-7} , which comes from the custom-made 5×10^{-6} filter combined with a reduction in aperture from 7.5 cm to 1.5 cm. We performed the solar disk ND observations between 05:23 and 05:27 UT (13:23 to 13:27 local time) when the Sun was at nearly the same altitude in the sky (within one degree) that it had been during totality – during the eclipse, the Sun was still rising, and during the ND observations, it was setting. Therefore, the atmospheric attenuation experienced during the calibration will be nearly identical to the time of the eclipse, ensuring the best possible absolute calibration. We chose to perform the ND calibration with the Fe X off-band telescope in particular due to the lower atmospheric scattering compared to the Fe XIV continuum wavelength, and due to the fact that the longer wavelengths (near Fe XI) typically have more issues with reflections introduced by the additional ND filter (e.g., Ghost images, see Section A.5).

We then fit the limb-darkening profile of the solar disk in the ND data, as shown in panel C of Figure A1. We found nearly the same limb-darkening coefficient we had with our older generation of telescopes in 2019 (see B. Boe et al. 2021). This fitting enabled a determination of the average solar disk brightness in units of pixel counts, as well as a determination of the size of the solar disk in the telescope. The solar disk data assisted in scaling the GONG H- α data prior to aligning the rotation, and determined the spatial scaling of helioprojective distance in the narrowband data. Once

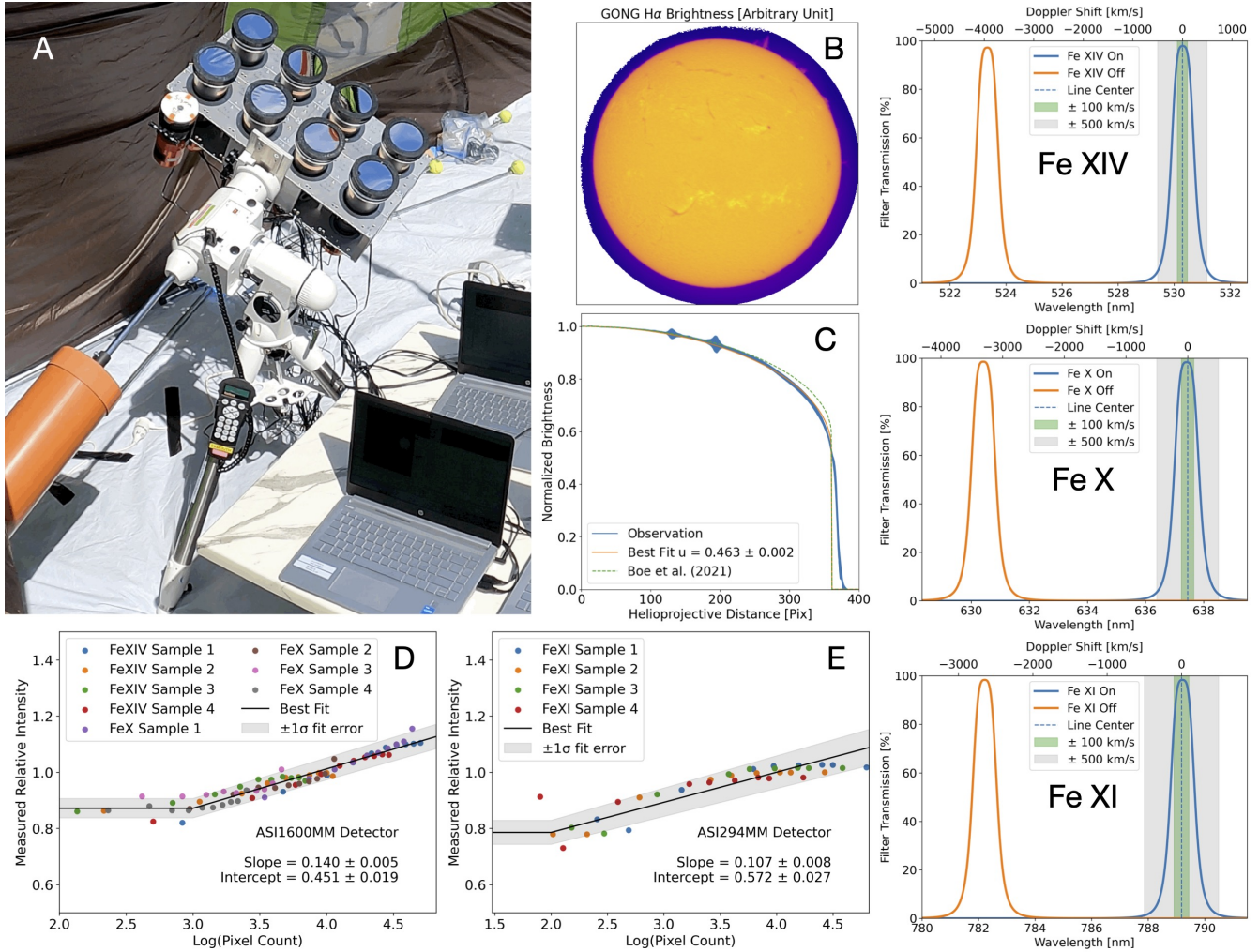


Figure A1. Collection of information about the instrumentation and calibration of the Narrowband telescope systems. Panel A shows an image of the telescope setup in Exmouth. Panel B shows the GONG H- α brightness at the time of totality. Panel C shows the radial trace of the solar disk brightness observed for the Fe X off-band ND observation used for absolutely calibrating the data. The right panels show the bandpasses for all the narrowband filters (on and off) for Fe XIV (top), Fe X (middle), and Fe XI (bottom). Panels D and E show the detector linearity data for the ASI1600MM and ASI294MM cameras, respectively.

the Fe XIV off-band had been calibrated into mean solar brightness units, we cross-calibrated the rest of the off-band observations (from both sites) using the observed brightness in a small region inside the largest streamer in the northeast (at about $1.1 R_{\odot}$ and 30 degrees position angle). Since the K-corona dominates in such regions, we can assume that the actual brightness is nearly identical between all continuum channels – whereas the F-corona dominates farther out and shows an increasing relative emission at longer wavelengths. Indeed, the relative emission between all continuum channels is rather consistent below about $1.5 R_{\odot}$, as shown in the bottom panels of Figure 8.

Finally, we accounted for the sky background in the continuum data by subtracting the brightness in the very corner of the FOV (at about $7.5 R_{\odot}$). The line

emission data do not need a background subtraction, as that is already accounted for in the off-band subtraction. However, for the continuum data, the sky brightness is not all of the signal even at that high helioprojective height. Thus, we first subtracted the background, then added back some brightness until the off-band Fe XIV brightness matched the LASCO-C2 brightness in the northwest streamer (about 340 PA at $6 R_{\odot}$), given how closely the LASCO-C2 brightness matched our calibrated data below about $4 R_{\odot}$. Assuming the LASCO-C2 brightness is relatively accurate, we found that the coronal continuum brightness was only 20 % of the total brightness at about $7.5 R_{\odot}$. That is, the sky brightness was 80% of the signal at that large height.

A.4. Detector Linearity

The new detectors used in this work (as described in Section 2) were all CMOS-style astrophotography detectors, designed for use by amateur astronomers. These detectors offer a rather high spatial resolution and FOV at an affordable price (given that several are needed for deployment at an eclipse), but they are not perfectly linear in their response. That is, the analog-to-digital converter in the camera is not completely uniform in its response depending on the number of counts in a given observation. To account for the non-linearity, we observed a constant light source from a calibration lamp with a large tungsten filament that was heated to a precise temperature (using a fixed current and voltage). We used an off-axis parabolic mirror in the lab to collimate light, simulating the same behavior as observing the Sun (i.e., a light source at infinity), and cycled over a range of exposure times to observe the exact same signal at different levels of saturation.

Next, we selected and averaged a number of specific regions containing hundreds of pixels over a perceptively uniform part of the filament structure in order to test how the signal varied as a function of total counts (via different exposure times). We did this experiment with an off-band telescope for all three ions to check for any wavelength dependence. The linearity data collected for the ASI1600MM camera is shown in panel D of Figure A1 for the Fe XIV and Fe X filters, and in panel E for the Fe XI filter and ASI294MM camera. In those plots, we show the relative signal of each region normalized based on the exposure time (relative to the signal at 10^4 counts) as a function of counts in log-space. Below about 1000 (100) counts, the ASI1600MM (ASI294MM) cameras do appear linear. However, as the counts increase, the relative intensity actually grows slightly. The ASI1600MM camera shows a more dramatic effect, with a change of about 30% over the dynamic range. We fit the data using a least-squares procedure, which is shown as the black line in the plots, with the $1\text{-}\sigma$ uncertainty on the fit shown as a grey bar. We corrected all data (the flats, eclipse images, and ND observations) using the fitted functions shown in the plots prior to further processing, which corrects for the linearity while preserving the photometric calibration.

A.5. Ghost Images

As with any optical system that has multiple glass surfaces, there are inevitably reflections that occur in our telescopic systems. There are two primary sources of reflections that occurred, one from the narrowband filter and the other from the lens. Both of these reflections originate as a secondary backward reflection of the orig-

inal reflection off the detector itself. These reflections can create “ghost” images that are superimposed on top of the original image (often referred to as a lens flare). Thankfully, these reflected images are rather faint, typically less than 0.1 – 1% of the original signal, but even that amount can create substantial problems if the reflected image of the low corona lands in a part of the original image that is far from the Sun.

To eliminate the filter ghost image entirely, we tilted the filters by 1.5 degrees relative to the optical axis, which results in the ghost image landing outside the FOV of the detector. The lens ghost is more difficult to correct for, as it still lands inside the FOV of our data. To account for this ghost image, we self-subtracted the data with a scaling factor, physical offset, rotation, magnification, and Gaussian blur optimized to remove the ghost image from each telescope’s data. The optimization was done painstakingly through a manual brute-force method (technique described in B. Boe et al. 2020) until the signature of the ghost image was minimized. Attempts were made to automate the procedure, but the phase correlation signal was too weak to obtain as optimal a removal as could be achieved manually. To account for possible bias due to this process, an additional photometric error equal to the brightness of the ghost image was added. Nevertheless, this additional error does not have a significant impact on the results presented in this work.

REFERENCES

- Akmal, A., Raymond, J. C., Vourlidis, A., et al. 2001, *ApJ*, 553, 922, doi: [10.1086/320971](https://doi.org/10.1086/320971)
- Altrock, R. C. 2011, *SoPh*, 274, 251, doi: [10.1007/s11207-011-9714-9](https://doi.org/10.1007/s11207-011-9714-9)
- Antonucci, E., Romoli, M., Andretta, V., et al. 2020, *A&A*, 642, A10, doi: [10.1051/0004-6361/201935338](https://doi.org/10.1051/0004-6361/201935338)
- Aschwanden, M. J., & Nitta, N. 2000, *ApJL*, 535, L59, doi: [10.1086/312695](https://doi.org/10.1086/312695)
- Auchère, F., Berghmans, D., Dumesnil, C., et al. 2023, *A&A*, 674, A127, doi: [10.1051/0004-6361/202346039](https://doi.org/10.1051/0004-6361/202346039)
- Boe, B., Downs, C., & Habbal, S. 2023a, *ApJ*, 951, 55, doi: [10.3847/1538-4357/acd10b](https://doi.org/10.3847/1538-4357/acd10b)
- Boe, B., Habbal, S., & Ding, A. 2023b, in *Bulletin of the American Astronomical Society*, Vol. 55, 032, doi: [10.3847/25c2cfef.fb89d0ac](https://doi.org/10.3847/25c2cfef.fb89d0ac)
- Boe, B., Habbal, S., Downs, C., & Druckmüller, M. 2021, *ApJ*, 912, 44, doi: [10.3847/1538-4357/abea79](https://doi.org/10.3847/1538-4357/abea79)
- Boe, B., Habbal, S., Downs, C., & Druckmüller, M. 2022, *ApJ*, 935, 173, doi: [10.3847/1538-4357/ac8101](https://doi.org/10.3847/1538-4357/ac8101)
- Boe, B., Habbal, S., Druckmüller, M., et al. 2020, *ApJ*, 888, 100, doi: [10.3847/1538-4357/ab5e34](https://doi.org/10.3847/1538-4357/ab5e34)
- Boe, B., Habbal, S., Druckmüller, M., et al. 2018, *ApJ*, 859, 155, doi: [10.3847/1538-4357/aabfb7](https://doi.org/10.3847/1538-4357/aabfb7)
- Brueckner, G. E., Howard, R. A., Koomen, M. J., et al. 1995, *SoPh*, 162, 357, doi: [10.1007/BF00733434](https://doi.org/10.1007/BF00733434)
- Cooper, J. F., Habbal, S. R., Angelopoulos, V., et al. 2023, in *Bulletin of the American Astronomical Society*, Vol. 55, 079, doi: [10.3847/25c2cfef.beac35c4](https://doi.org/10.3847/25c2cfef.beac35c4)
- Deforest, C., Killough, R., Gibson, S., et al. 2022, in 2022 IEEE Aerospace Conference, 1–11, doi: [10.1109/AERO53065.2022.9843340](https://doi.org/10.1109/AERO53065.2022.9843340)
- Del Zanna, G. 2025, *MNRAS*, 543, 390, doi: [10.1093/mnras/staf1401](https://doi.org/10.1093/mnras/staf1401)
- Del Zanna, G., & Mason, H. E. 2018, *Living Reviews in Solar Physics*, 15, 5, doi: [10.1007/s41116-018-0015-3](https://doi.org/10.1007/s41116-018-0015-3)
- Dere, K. P., Landi, E., Mason, H. E., Monsignori Fossi, B. C., & Young, P. R. 1997, *A&AS*, 125, 149, doi: [10.1051/aas:1997368](https://doi.org/10.1051/aas:1997368)
- Ding, A., & Habbal, S. R. 2017, *ApJL*, 842, L7, doi: [10.3847/2041-8213/aa7460](https://doi.org/10.3847/2041-8213/aa7460)
- Druckmüller, M. 2009, *ApJ*, 706, 1605, doi: [10.1088/0004-637X/706/2/1605](https://doi.org/10.1088/0004-637X/706/2/1605)
- Druckmüller, M., Rušin, V., & Minarovjech, M. 2006, *Contributions of the Astronomical Observatory Skalnaté Pleso*, 36, 131
- Dufresne, R. P., Del Zanna, G., Young, P. R., et al. 2024, *ApJ*, 974, 71, doi: [10.3847/1538-4357/ad6765](https://doi.org/10.3847/1538-4357/ad6765)
- Edlén, B. 1943, *ZA*, 22, 30
- Esser, R., Fineschi, S., Dobrzycka, D., et al. 1999, *ApJL*, 510, L63, doi: [10.1086/311786](https://doi.org/10.1086/311786)
- Galano, D., Bemporad, A., Buckley, S., et al. 2018, in *Society of Photo-Optical Instrumentation Engineers (SPIE) Conference Series*, Vol. 10698, Proc. SPIE, 106982Y, doi: [10.1117/12.2312493](https://doi.org/10.1117/12.2312493)
- Gary, D. E. 2023, *ARA&A*, 61, 427, doi: [10.1146/annurev-astro-071221-052744](https://doi.org/10.1146/annurev-astro-071221-052744)
- Gary, D. E., Fleishman, G. D., & Nita, G. M. 2013, *SoPh*, 288, 549, doi: [10.1007/s11207-013-0299-3](https://doi.org/10.1007/s11207-013-0299-3)
- Gibson, S. E., Dalmasse, K., Rachmeler, L. A., et al. 2017, *ApJL*, 840, L13, doi: [10.3847/2041-8213/aa6fac](https://doi.org/10.3847/2041-8213/aa6fac)
- Giordano, S., Ciaravella, A., Raymond, J. C., Ko, Y. K., & Suleiman, R. 2013, *Journal of Geophysical Research (Space Physics)*, 118, 967, doi: [10.1002/jgra.50166](https://doi.org/10.1002/jgra.50166)
- Giordano, S., Spadaro, D., Susino, R., et al. 2025, *A&A*, 701, A56, doi: [10.1051/0004-6361/202554105](https://doi.org/10.1051/0004-6361/202554105)
- Grottrian, W. 1939, *Naturwissenschaften*, 27, 214, doi: [10.1007/BF01488890](https://doi.org/10.1007/BF01488890)
- Guhathakurta, M., Rottman, G. J., Fisher, R. R., Orrall, F. Q., & Altrock, R. C. 1992, *ApJ*, 388, 633, doi: [10.1086/171180](https://doi.org/10.1086/171180)
- Habbal, S. R., Druckmüller, M., Morgan, H., et al. 2010a, *ApJ*, 719, 1362, doi: [10.1088/0004-637X/719/2/1362](https://doi.org/10.1088/0004-637X/719/2/1362)
- Habbal, S. R., Morgan, H., Druckmüller, M., & Ding, A. 2010b, *ApJL*, 711, L75, doi: [10.1088/2041-8205/711/2/L75](https://doi.org/10.1088/2041-8205/711/2/L75)
- Habbal, S. R., Morgan, H., Druckmüller, M., et al. 2013, *SoPh*, 285, 9, doi: [10.1007/s11207-012-0115-5](https://doi.org/10.1007/s11207-012-0115-5)
- Habbal, S. R., Morgan, H., Johnson, J., et al. 2007, *ApJ*, 663, 598, doi: [10.1086/518403](https://doi.org/10.1086/518403)
- Habbal, S. R., Druckmüller, M., Morgan, H., et al. 2010c, *ApJ*, 708, 1650, doi: [10.1088/0004-637X/708/2/1650](https://doi.org/10.1088/0004-637X/708/2/1650)
- Habbal, S. R., Druckmüller, M., Morgan, H., et al. 2011, *ApJ*, 734, 120, doi: [10.1088/0004-637X/734/2/120](https://doi.org/10.1088/0004-637X/734/2/120)
- Habbal, S. R., Druckmüller, M., Alzate, N., et al. 2021, *ApJL*, 911, L4, doi: [10.3847/2041-8213/abe775](https://doi.org/10.3847/2041-8213/abe775)
- Hahn, M., Fu, X., Hofmeister, S. J., et al. 2025, *ApJ*, 984, 69, doi: [10.3847/1538-4357/adc1c0](https://doi.org/10.3847/1538-4357/adc1c0)
- Harvey, J. W., Hill, F., Hubbard, R. P., et al. 1996, *Science*, 272, 1284, doi: [10.1126/science.272.5266.1284](https://doi.org/10.1126/science.272.5266.1284)
- Hill, F. 2018, *Space Weather*, 16, 1488, doi: [10.1029/2018SW002001](https://doi.org/10.1029/2018SW002001)
- Hyder, C. L., & Lites, B. W. 1970, *SoPh*, 14, 147, doi: [10.1007/BF00240170](https://doi.org/10.1007/BF00240170)
- Ko, Y.-K., Fisk, L. A., Geiss, J., Gloeckler, G., & Guhathakurta, M. 1997, *SoPh*, 171, 345, doi: [10.1023/A:1004943213433](https://doi.org/10.1023/A:1004943213433)

- Kohl, J. L., Esser, R., Gardner, L. D., et al. 1995, *SoPh*, 162, 313, doi: [10.1007/BF00733433](https://doi.org/10.1007/BF00733433)
- Kohl, J. L., Noci, G., Antonucci, E., et al. 1997, *SoPh*, 175, 613, doi: [10.1023/A:1004903206467](https://doi.org/10.1023/A:1004903206467)
- Kohl, J. L., Noci, G., Antonucci, E., et al. 1998, *ApJL*, 501, L127, doi: [10.1086/311434](https://doi.org/10.1086/311434)
- Koutchmy, S., Baudin, F., Abdi, S., Golub, L., & Sèvre, F. 2019, *A&A*, 632, A86, doi: [10.1051/0004-6361/201935681](https://doi.org/10.1051/0004-6361/201935681)
- Lamy, P., Barlyaeva, T., Llebaria, A., & Floyd, O. 2014, *Journal of Geophysical Research (Space Physics)*, 119, 47, doi: [10.1002/2013JA019468](https://doi.org/10.1002/2013JA019468)
- Lamy, P., Llebaria, A., Boclet, B., et al. 2020, *SoPh*, 295, 89, doi: [10.1007/s11207-020-01650-y](https://doi.org/10.1007/s11207-020-01650-y)
- Landi, E., & Landini, M. 1997, *A&A*, 327, 1230
- Lin, H., Kuhn, J. R., & Coulter, R. 2004, *ApJL*, 613, L177, doi: [10.1086/425217](https://doi.org/10.1086/425217)
- Llebaria, A., Loirat, J., & Lamy, P. 2012, in *Society of Photo-Optical Instrumentation Engineers (SPIE) Conference Series*, Vol. 8442, *Space Telescopes and Instrumentation 2012: Optical, Infrared, and Millimeter Wave*, ed. M. C. Clampin, G. G. Fazio, H. A. MacEwen, & J. M. Oschmann, Jr., 844226, doi: [10.1117/12.926215](https://doi.org/10.1117/12.926215)
- Lyot, B. 1939, *MNRAS*, 99, 580, doi: [10.1093/mnras/99.8.580](https://doi.org/10.1093/mnras/99.8.580)
- Mann, I. 1998, *Earth, Planets and Space*, 50, 465, doi: [10.1186/BF03352135](https://doi.org/10.1186/BF03352135)
- Maunder, E. W. 1899, *The Indian eclipse, 1898 : report of the expeditions organized by the British Astronomical Association to observe the total solar eclipse of 1898 January 22*
- Mierla, M., Schwenn, R., Teriaca, L., Stenborg, G., & Podlipnik, B. 2008, *A&A*, 480, 509, doi: [10.1051/0004-6361:20078329](https://doi.org/10.1051/0004-6361:20078329)
- Morgan, H., & Habbal, S. R. 2007, *A&A*, 471, L47, doi: [10.1051/0004-6361:20078071](https://doi.org/10.1051/0004-6361:20078071)
- Morton, R. J., Molnar, M., Cranmer, S. R., & Schad, T. A. 2025, *ApJ*, 982, 104, doi: [10.3847/1538-4357/adb8df](https://doi.org/10.3847/1538-4357/adb8df)
- Muro, G. D., Gunn, M., Fearn, S., Fearn, T., & Morgan, H. 2023, *SoPh*, 298, 75, doi: [10.1007/s11207-023-02162-1](https://doi.org/10.1007/s11207-023-02162-1)
- Muthu Priyal, V., Ramesh, R., Singh, J., & Sasikumar Raja, K. 2025, *ApJ*, 983, 171, doi: [10.3847/1538-4357/adbe73](https://doi.org/10.3847/1538-4357/adbe73)
- Nakagawa, A. 2008, *ApJ*, 674, 1167, doi: [10.1086/524885](https://doi.org/10.1086/524885)
- Oloketuyi, J., Liu, Y., Deng, L., et al. 2024, *ApJS*, 275, 3, doi: [10.3847/1538-4365/ad746a](https://doi.org/10.3847/1538-4365/ad746a)
- Pagot, E., Lamy, P., Llebaria, A., & Boclet, B. 2014, *SoPh*, 289, 1433, doi: [10.1007/s11207-013-0402-9](https://doi.org/10.1007/s11207-013-0402-9)
- Ramesh, R., Muthu Priyal, V., Singh, J., et al. 2024, *ApJL*, 976, L6, doi: [10.3847/2041-8213/ad8c45](https://doi.org/10.3847/2041-8213/ad8c45)
- Raouafi, N. E., Riley, P., Gibson, S., Fineschi, S., & Solanki, S. K. 2016, *Frontiers in Astronomy and Space Sciences*, 3, 20, doi: [10.3389/fspas.2016.00020](https://doi.org/10.3389/fspas.2016.00020)
- Raymond, J. C., Kohl, J. L., Noci, G., et al. 1997, *SoPh*, 175, 645, doi: [10.1023/A:1004948423169](https://doi.org/10.1023/A:1004948423169)
- Reginald, N., Newmark, J., & Rastaetter, L. 2023, *SoPh*, 298, 73, doi: [10.1007/s11207-023-02160-3](https://doi.org/10.1007/s11207-023-02160-3)
- Rimmele, T. R., Warner, M., Keil, S. L., et al. 2020, *SoPh*, 295, 172, doi: [10.1007/s11207-020-01736-7](https://doi.org/10.1007/s11207-020-01736-7)
- Romoli, M., Antonucci, E., Andretta, V., et al. 2021, *A&A*, 656, A32, doi: [10.1051/0004-6361/202140980](https://doi.org/10.1051/0004-6361/202140980)
- Russano, G., Andretta, V., De Leo, Y., et al. 2024, *A&A*, 683, A191, doi: [10.1051/0004-6361/202347741](https://doi.org/10.1051/0004-6361/202347741)
- Rybansky, M., Rusin, V., Gaspar, P., & Altrock, R. C. 1994, *SoPh*, 152, 487, doi: [10.1007/BF00680452](https://doi.org/10.1007/BF00680452)
- Samra, J. E., Del Zanna, G., Elizalde Flores, C., Madsen, C., & DeLuca, E. 2025, *ApJ*, 992, 145, doi: [10.3847/1538-4357/ae046a](https://doi.org/10.3847/1538-4357/ae046a)
- Samra, J. E., Madsen, C. A., Cheimets, P., et al. 2022a, *ApJ*, 933, 82, doi: [10.3847/1538-4357/ac6ce8](https://doi.org/10.3847/1538-4357/ac6ce8)
- Samra, J. E., Marquez, V., Cheimets, P., et al. 2022b, *AJ*, 164, 39, doi: [10.3847/1538-3881/ac7218](https://doi.org/10.3847/1538-3881/ac7218)
- Schad, T. A., Petrie, G., Kuhn, J., et al. 2024a, *Science Advances*, 10, eadq1604, doi: [10.1126/sciadv.adq1604](https://doi.org/10.1126/sciadv.adq1604)
- Schad, T. A., Fehlmann, A., Dima, G. I., et al. 2024b, *ApJ*, 965, 40, doi: [10.3847/1538-4357/ad2995](https://doi.org/10.3847/1538-4357/ad2995)
- Seaton, D. B., Hughes, J. M., Tadikonda, S. K., et al. 2021, *Nature Astronomy*, 5, 1029, doi: [10.1038/s41550-021-01427-8](https://doi.org/10.1038/s41550-021-01427-8)
- Seaton, D. B., Downs, C., Del Zanna, G., et al. 2025, *ApJ*, 985, 89, doi: [10.3847/1538-4357/adcab5](https://doi.org/10.3847/1538-4357/adcab5)
- Singh, J., Saxena, A. K., & Bappu, M. K. V. 1982, *Journal of Astrophysics and Astronomy*, 3, 249, doi: [10.1007/BF02714865](https://doi.org/10.1007/BF02714865)
- Srivastava, N., Schwenn, R., Inhester, B., Martin, S. F., & Hanaoka, Y. 2000, *ApJ*, 534, 468, doi: [10.1086/308749](https://doi.org/10.1086/308749)
- Suleiman, R. M., Kohl, J. L., Panasyuk, A. V., et al. 1999, *SSRv*, 87, 327, doi: [10.1023/A:1005102013262](https://doi.org/10.1023/A:1005102013262)
- Supriya, H. D., Trujillo Bueno, J., de Vicente, Á., & del Pino Alemán, T. 2021, *ApJ*, 920, 140, doi: [10.3847/1538-4357/ac1068](https://doi.org/10.3847/1538-4357/ac1068)
- Thompson, B. J., Qiu, J., Lugaz, N., & Webb, D. F. 2021, in *Solar Physics and Solar Wind*, ed. N. E. Raouafi & A. Vourlidas, Vol. 1, 179, doi: [10.1002/9781119815600.ch5](https://doi.org/10.1002/9781119815600.ch5)
- Tomczyk, S., McIntosh, S. W., Keil, S. L., et al. 2007, *Science*, 317, 1192, doi: [10.1126/science.1143304](https://doi.org/10.1126/science.1143304)
- Tomczyk, S., Card, G. L., Darnell, T., et al. 2008, *SoPh*, 247, 411, doi: [10.1007/s11207-007-9103-6](https://doi.org/10.1007/s11207-007-9103-6)

- Tomczyk, S., Landi, E., Berkey, B., et al. 2022, in AGU Fall Meeting Abstracts, Vol. 2022, AGU Fall Meeting Abstracts, SH25D–2078
- van de Hulst, H. C. 1950, BAN, 11, 135
- Viall, N. M., De Moortel, I., Downs, C., et al. 2021, in Solar Physics and Solar Wind, ed. N. E. Raouafi & A. Vourlidas, Vol. 1, 35, doi: [10.1002/9781119815600.ch210.1002/essoar.10502697.1](https://doi.org/10.1002/9781119815600.ch210.1002/essoar.10502697.1)
- Vourlidas, A., Howard, R. A., Plunkett, S. P., et al. 2016, SSRv, 204, 83, doi: [10.1007/s11214-014-0114-y](https://doi.org/10.1007/s11214-014-0114-y)
- Wang, Y. M., Sheeley, N. R., J., Hawley, S. H., et al. 1997, ApJ, 485, 419, doi: [10.1086/304405](https://doi.org/10.1086/304405)
- West, M. J., Seaton, D. B., Wexler, D. B., et al. 2023, SoPh, 298, 78, doi: [10.1007/s11207-023-02170-1](https://doi.org/10.1007/s11207-023-02170-1)
- Withbroe, G. L., Kohl, J. L., Weiser, H., & Munro, R. H. 1982, SSRv, 33, 17, doi: [10.1007/BF00213247](https://doi.org/10.1007/BF00213247)
- Young, C. A. 1872, Nature, 7, 28, doi: [10.1038/007028b0](https://doi.org/10.1038/007028b0)
- Zangrilli, L., & Poletto, G. 2012, A&A, 545, A8, doi: [10.1051/0004-6361/201219452](https://doi.org/10.1051/0004-6361/201219452)
- Zhu, Y., Habbal, S. R., Ding, A., et al. 2024, ApJ, 966, 122, doi: [10.3847/1538-4357/ad3424](https://doi.org/10.3847/1538-4357/ad3424)
- Zhukov, A. N., Dolla, L., Mierla, M., et al. 2025, arXiv e-prints, arXiv:2511.01679, doi: [10.48550/arXiv.2511.01679](https://doi.org/10.48550/arXiv.2511.01679)